Modelling DC Collection of Offshore Wind Farms for Harmonic Susceptibility Study

Project Report

Group WPS2 – 830

Aalborg University
MSc Energy Engineering

Energy Engineering
Aalborg University
http://www.aau.dk

AALBORG UNIVERSITY
STUDENT REPORT

Title:
Modelling DC Collection of Offshore Wind Farms for Harmonic Susceptibility Study

Theme:
Wind Power Systems

Project Period:
Spring Semester 2017

Project Group:
WPS2/830

Participant(s):
Carlos Imbaquingo
Nicola Isernia
Eduard Sarrà
Alberto Tonellotto

Supervisor(s):
Philip Kjær
Yu-Hsing Chen

Copies: 1

Page Numbers: 71

Date of Completion:
May 28, 2017

Abstract:

Offshore wind farms with DC collection present an advantage on efficiency and costs over long distances compared to AC transmission. A major problem in their development is the susceptibility of the power collection grid to harmonic disturbances. In this report a simplified and reliable method to perform an harmonic susceptibility study is proposed. A resonant converter topology for high power DC/DC conversion has been investigated by the means of discrete time modelling technique. Then, a suitable controller for the converter has been designed. Simplified model of the converter and controller has been verified by comparison to an accurate switching model. The frequency dependent behaviour of the cables has been taken into account for the network study. The proposed model results show a good matching with the switching model simulations and laboratory tests for frequencies sufficiently above the resonant frequency of the output filter of the converter. The accordance with simulations is good also at low frequency for clusters of few wind turbines. In conclusion, the proposed method could be used to perform a susceptibility study in an early stage of the network project. As a final verification, it is recommended to perform the study by the switching model of the converters.

Contents

Glossary

α, β	Conducting space angles	[rad]
ω_c	Crossover angular frequency	[rad/s]
ω_r	Resonant angular frequency	[rad/s]
ω_{rs}	Ratio between resonant and switching angular frequency	[rad/s]
ω_s	Switching angular frequency	[rad/s]
C_f	Filter capacitance	[F]
C_r	Resonant tank capacitance	[F]
$D_{5,6,7,8}$	Diodes of the rectifier	[–]
D_{aux}	Auxiliary diode for experimental work	[–]
f_r	Resonant frequency	[Hz]
f_s	Switching frequency	[Hz]
f_{sw_op}	Operating point switching frequency	[Hz]
f_{sw_ss}	Small signal switching frequency	[Hz]
$\tilde{I}_{eq}$	Harmonic equivalent model amplitude current	[A]
i_n	Output filter current	[A]
$i_{n,REF}$	Reference output filter current	[A]
I_{out}	Output rectifier current	[A]
i_r	Resonant tank current	[A]
$\tilde{I}_{sw}$	Switching model amplitude current	[A]
L_f	Filter inductance	[H]
L_m	Magnetizing inductance	[H]
L_r	Resonant tank inductance	[H]
N_1	Number of winding turns on the primary side of transformer	[–]
N_2	Number of winding turns on the secondary side of transformer	[–]
P_o	Output power	[W]
P_{ref}	Reference power	[W]
q	Tank capacitor charge	[C]
R_c	Filter capacitor resistance	[Ω]
R_L	Filter inductor resistance	[Ω]
$T_{1,2,3,4}$	Switches of the inverter	[–]
T_r	Resonant period	[s]
$T_s = T_{sw}$	Switching period	[s]
$V_c = V_{cr}$	Tank capacitor voltage	[V]
V_g	Primary transformer voltage	[V]
V_g'	Secondary transformer voltage	[V]
V_{LVDC}	Low DC voltage	[V]
V_{MVDC}	Medium DC voltage	[V]
V_n	Output filter voltage	[V]
V_o	Output rectifier voltage	[V]
Z_r	Resonant impedance	[Ω]

Chapter 1

Introduction

In the recent years, offshore wind energy has been developing fast. A total of 3,230 wind turbines were installed by 2015 and connected to the electricity grid in the European continent. Total installed capacity has reached 11.027 GW, enough to cover almost 1% of the EU's total electricity consumption and has been growing with a compound annual growth rate of 31% in the last 5 years.[1]

Offshore wind farms with DC collection are being investigated due to its advantages on cost and efficiency.[12]. Nowadays, one of the main goals is to reduce the cost of the network between the wind turbines and the onshore grid. A DC collection grid (described in section 1.1) consists on a high power DC/DC converter, submarine cables and an offshore substation. Current harmonics could appear into the grid due to the operation of the offshore substation converter. This is one of the major issues for the development of the DC power collection network, as resonant phenomena could affect badly the operation of the converters. Thus, the main objective of the project is to develop a methodology to study the harmonic susceptibility in offshore wind farms.

High power DC/DC converters are needed to transform the voltage within the grid, and different types of DC/DC converters with hard switching topologies have been studied for wind farms applications. [8]

However, a DC/DC converter based on the Series Resonant Converter (SRC) is proposed as an efficient and cost effective type due to its soft-switching characteristics.[9] A SRC converter with the resonant tank on the secondary and a new control technique side is here considered, named SRC# (investigated at Department of Energy Technology in Aalborg University [4], [10]). All the models and methodologies presented in this report will be tested in PLECS simulations for a cluster of seven wind turbines connected to an offshore substation, through submarine cables. This study case is described in detail in section 1.1

Before a harmonic susceptbibility study can be performed, some modeling steps are required, and the structure of the report is here presented:

- Chapter 2 presents a literature review, discrete time modeling technique is used to model the turbine DC/DC converter and investigate its operating points;
- In chapter 3, the controller design for the converter is presented. In order to accomplish this aim, a linearization of the SRC# model is performed, and the interaction with the LC output is taken into account. Validation of the small signal model in open and closed loop are also presented, via comparison with PLECS simulations. Filter design and the validation of the converter and the controller model is illustrated. Then, the frequency dependent model of the turbine DC/DC converter (SRC#) is evaluated for a specific frequency, in order to develop a simple admittance equivalent circuit, representing a simplified and reliable method to analyze the network.
- In chapter 4, a harmonic susceptibility study is finally performed for the chosen study case, in order to observe how voltage harmonics from the offshore substation could affect the converter and the DC power collection grid. First the model of the cables is described. A working point is therefore chosen, and the developed model results are compared with the accurate switching model simulations performed in PLECS. The results of the simulations obtained with software PLECS are then commented.
- Chapter 5 presents a scaled-down setup of the converter to verify the previously mentioned model and the developed controller. A comparison between the results obtained with the test setup, PLECS simulations and the small signal harmonic model is also presented.
- Finally, chapter 6 exposes the conclusions achieved from results in chapter 3, chapter 4 and chapter 5.

1.1 Study Case

The alternative DC collection is still an immature technology and it requires more research. The harmonic pollution is one of the major issues when the wind farm is composed by a large amount of wind turbines.

The study system of the present project is depicted in Figure 1.1. The project focuses on the MVDC wind farm power collection which is composed by DC/DC converters, an MVDC array network and the offshore substation platform. Also the HVDC transmission line, the onshore substation and the AC grid are depicted in Figure 1.1.

The DC network configuration consists in a cluster of 7 wind turbines connected in parallel to a submarine cable, as shown in Figure 1.2. Length of the cables is 820m among each wind turbine and between the first wind turbine and the offshore substation. Harmonics caused by this substation can cause undesirable resonant phenomena and raise stability issues.

The DC network will be modelled in PLECS with an equivalent model for the cables. Each wind turbine will be represented by an admittance as described in section 3.6, considering the behaviour of the converter and the filter. Finally, the offshore substation perturbation is represented as an AC source with variable frequency.

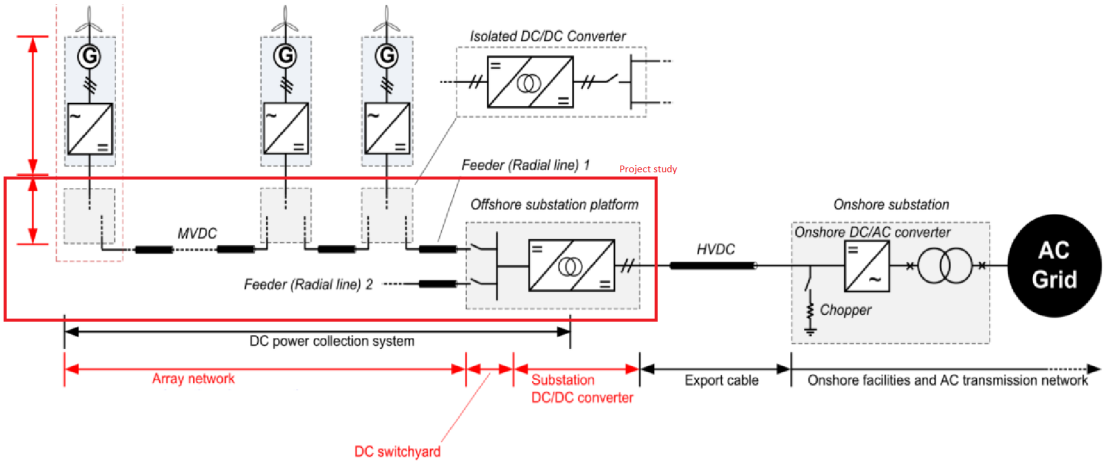

Figure 1.1: Wind farm network schematic [10]

In Table 1.1, main parameters of the converters considered in the study case are presented.

Table 1.1: Parameters of the SRC# for state-space model and circuit simulation model

Low Voltage DC (V_{LVDC})	$4.04(kV_{DC})$
Medium Voltage DC (V_{MVDC})	$100.0(kV_{DC})$
Transformer winding voltage ratio $(N1 : N2)$	$1 : 25$
Rated output power	$10(MW)$
Resonant inductor L_r	$78.1(mH)$
Resonant capacitor C_r	$0.25(uF)$

The MVDC cables illustrated in Figure 1.1 are used to connect the wind turbines in parallel, which are then connected to the offshore substation platform through J-tube. [7]. They are formed of several layers depicted in Figure 1.3 and they have a length of 820m. Each part of the cable has a specific function and cables are sized considering the network stresses. Radius of each layer is illustrated in Table 1.2. There are two types of cables represented in Figure 1.2. The first four cables, with a $100mm^2$ cross-sectional area of the inner conductor are named cable2 and they carry ta lower current. The last three ones, with a $300mm^2$ cross-sectional area, carrying a higher current, are named cable 2.

However, in this project, the design of the MVDC cables is not considered. Regarding the offshore substation, its main goal is to transform the voltage from the wind turbines to a higher voltage level before delivering it to the onshore grid. Moreover, a DC collection wind farm requires one less step conversion compared to an AC collection which means that only one MVDC/HVDC offshore substation is needed, instead of the two in AC wind farms, MVAC/HVAC and HVAC/HVDC substation conversions.

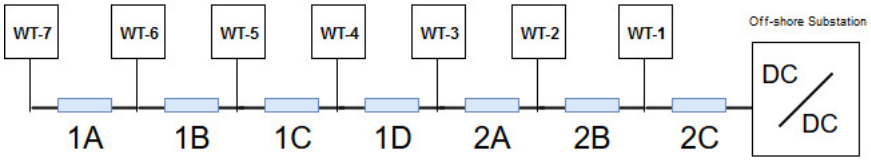

Figure 1.2: Schematic of the Schematic

Table 1.2: Geometry parameters of the cables

Radius	Cable 1	Cable 2
Conductor	0.564*cm*	0.977*cm*
*Insulator*1	1.934*cm*	2.537*cm*
Sheath	2.134*cm*	2.767*cm*
*Insulator*2	2.284*cm*	2.937*cm*
Armour	2.534*cm*	3.252*cm*
*Insulator*3	2.814*cm*	3.582*cm*

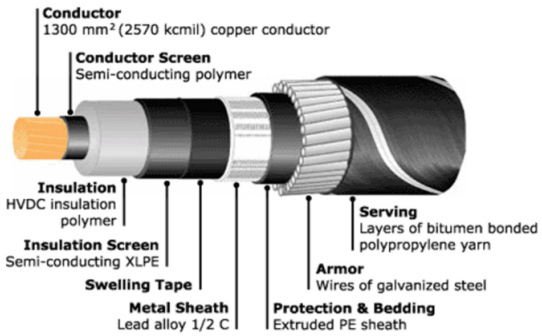

Figure 1.3: Structure of the MVDC submarine cables. Cable composed by: conductor layer, insulation system, water-blocking sheath (metal sheath), armour and serving.[7]

Chapter 2

SRC# Operation and Modeling

Before going into the details of converter models, main motivations leading to the choice of the SRC# will be presented. A mathematical model will be developed by means of discrete time modeling. Further description is presented to show how to find the operating conditions of the converter.

2.1 Series Resonant Converter

Similarly to the SRC, the SRC# is made-up of a full-bridge inverter, step-up transformer, a LC tank, a diode rectifier, and an output filter. However, the LC tank is placed in the secondary part of the transformer as it is shown in Figure 2.1.

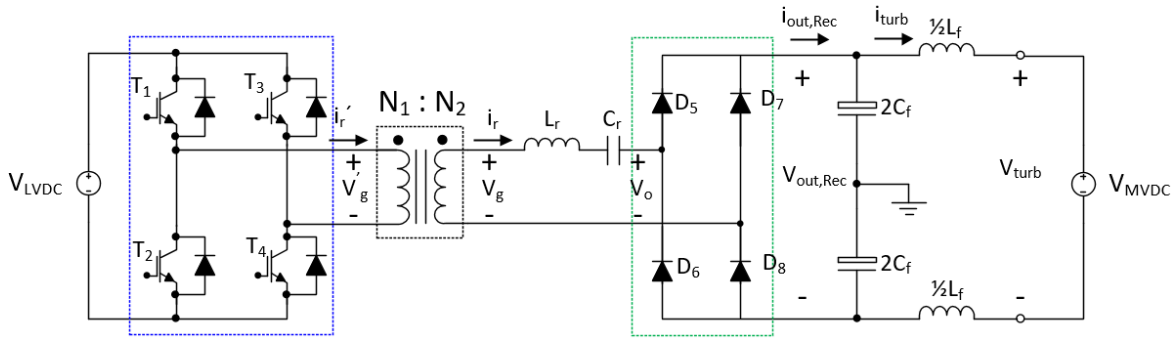

Figure 2.1: Structure of the SRC# [10]

The full-bridge inverter, is used on the turbine side in order to obtain a quasi-square voltage. Then, a step-up transformer increases the voltage to the grid side level. The quasi-square waveform voltage excites the LC tank, which brings about a current flow that is almost sinusoidal. Finally, the diode rectifier and the filter transform back this AC current into DC current on the grid side.

To allow the soft-switching of the IGBTs at turn off, the SRC# is set to work in sub-resonant mode operation. This means that the switching frequency is always smaller than the resonant frequency of the LC tank. The pulse removal control technique is used to govern the converter, as described below and shown in Figure 2.2 for Discontinuous Conduction Mode (DCM). The switches of the same leg are pulsed alternatively with a duty ratio equal to 0.5, and the trigger pulses for T_3 and T_4 are phase-delayed by a time interval of $T_r/2$ with regard to T_1 and T_2 respectively. As a result, a quasi-square voltage waveform v_g is created. When T_1 and T_4 are conducting together, the applied voltage excites the LC tank, leading to a sinusoidal tank current i_r at the resonant frequency. This current will cross the zero value after half resonant cycle, turning off the IGBTs. The switch T_3 is already pulsed in this time instant, leading the current to be zero as the voltage applied on the turbine side of the transformer.

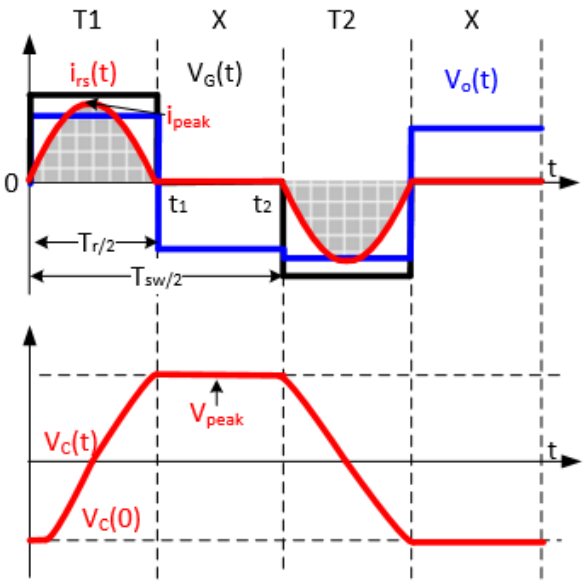

Figure 2.2: Waveforms in DCM1 operation. [10]

Independently of the switching frequency, the DC voltage at the primary side of the transformer is applied for a time interval equal to half resonant period. This way, the magnetizing current never increases above a certain value, even if the switching frequency becomes smaller. Therefore, magnetic saturation is avoided, and the transformer could be sized for higher operating frequency. This is probably the main advantage of SRC# respect to classical SRC.

Moreover, the switches are naturally turned off by the zero-crossing of the current, which lowers switching losses. This fact justifies the choice of running the converter in sub-resonant mode. Nonetheless, DCM operation of the SRC# leads to an approximate linear relationship between power flow and switching frequency.

From the tank current waveform introduced in Figure 2.2, the mean current delivered at the grid side is calculated by Equation 2.1.

$$I_{out} = < |i_r| >_{T_s} = \frac{2q}{T_s} \tag{2.1}$$

where q is the charge brought into the capacitor by the tank current during a half cycle of the resonant period. This charge value is linked with the peak value of the voltage across the tank capacitor, by Equation 2.2. The voltage v_g has to be higher than v_o; otherwise, the

diode bridge would result always reverse-biased with zero current and power flow.

$$q = 2 \cdot C_r \cdot V_{Cr} \tag{2.2}$$

Moreover, DCM occurs when the voltage across the capacitor, at the end of half resonant period, equals the voltage magnitude on the grid side. Thus, the linear relationship between switching frequency and active power flow is found with Equation 2.3

$$P_{out} = V_{out} I_{out} = 4\ C_r\ V_{out}^2\ f_{sw} \tag{2.3}$$

In order to operate in sub-resonant mode, the inductance and capacitance of the LC tank are chosen according to the nominal operating frequency.

$$L_r C_r > \frac{1}{(2\pi f_r)^2} \tag{2.4}$$

Main advantages of SRC# are summarized as follows:

- Small transformer, sized for the higher operating frequency.
- Zero current switching of IGBTs at turn off; thus, low switching losses leading to high efficiency.
- Linear relation between switching frequency and active power flow.

2.2 SRC# Operation Mode

In the section 2.1 is only mentioned the DCM of the converter. However, the SRC# operated in sub-resonant mode is likely to operate in an hybrid conduction mode, similar to DCM but somehow more complicated. The operating switching frequency will be always lower than the resonant frequency, and higher than half of the resonant frequency, in our modeling, as described by Equation 2.5.

$$\frac{f_r}{2} < f_s < f_r \tag{2.5}$$

In order to understand all modes of operation, the tank current and input voltage waveforms are considered in Figure 2.3.

- In the first subinterval, the IGBTs T_1 and T_4 are conducting together with the diodes D_5 and D_8 of the rectifier. The generic situation in which the initial current value is non-zero is considered. An equivalent circuit is shown in Figure 2.4(a). The tank current is a sine wave at the resonant frequency which has a zero crossing within half cycle of the resonant period.

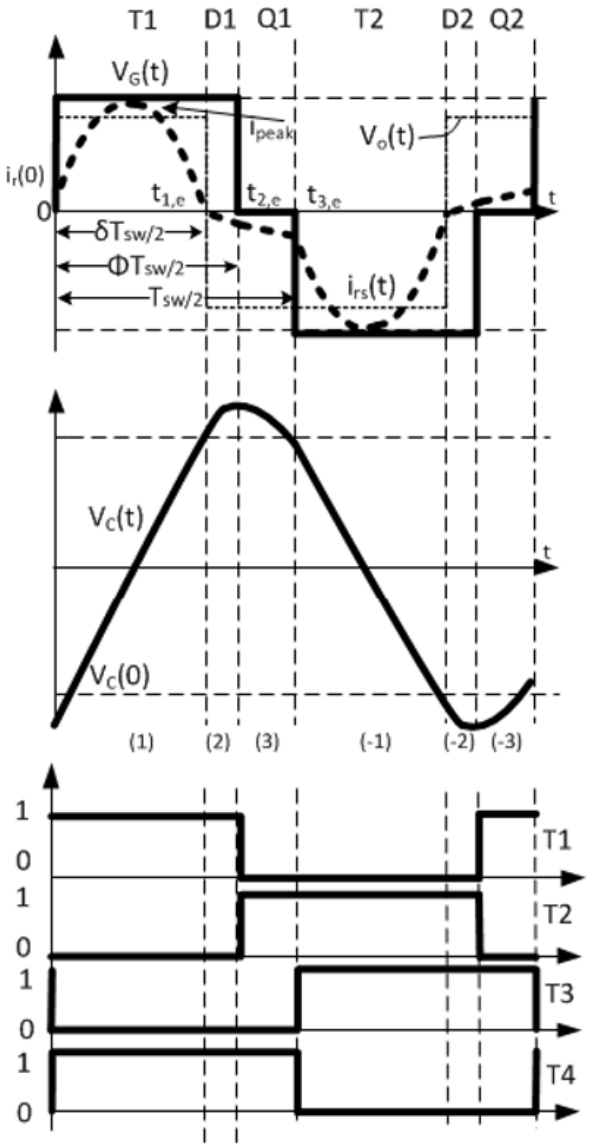

Figure 2.3: Waveforms for SRC# of the tank current and voltages. [4]

- In the second interval, IGBTs T_1 and T_4 are still on but stop their conduction, because the current naturally becomes zero. Diodes D_1 and D_4 can start conducting a negative current if the diode bridge rectifier is forward-biased. This generic situation and an equivalent circuit for this sub-interval are depicted in Figure 2.4(b).
- After a time delay, IGBT T_3 is turned on, according to the pulse removal control technique, which results in the third sub-interval. The applied voltage on the turbine side of the transformer is zero, while the voltage $-V_o$ appears on the bridge rectifier because diodes D_6 and D_7 conduct. An equivalent circuit is described in

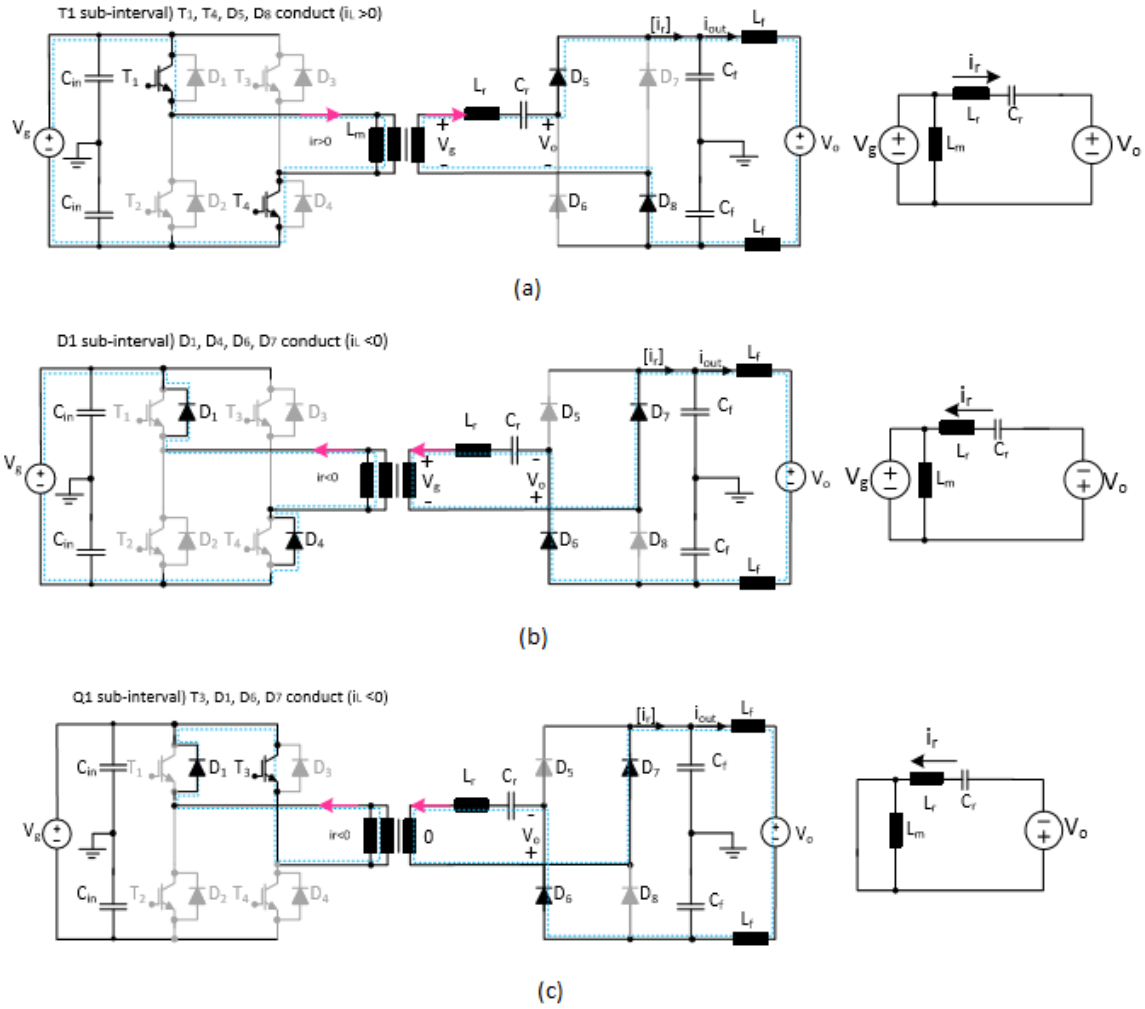

Figure 2.4: Equivalent Circuits for different subintervals during event k_{th}: (a)$T_1 - T_4$; (b)$D_1 - D_4$; (c)$D_1 - T_3$ [10]

Figure 2.4(c).

- Afterwards, the IGBT T_2 is turned on, leading to a similar series of subintervals with opposite polarities of voltages and tank current.

It is worth to mention that the second sub-interval does not generally occur, unless the voltage gap between the turbine side and the grid side is high, e.g. fault situations. In normal operation conditions, zero tank current and fixed voltage across the tank capacitor are observed after the natural zero crossing of the tank current. Thus, the second sub-interval undergoes a non-conducting state defined as X. No current goes through the tank and no voltage drops across the inductor. This operation mode is called CCM1-Hybrid,

its waveforms are depicted in Figure 2.5 and will represent the reference to model the converter.

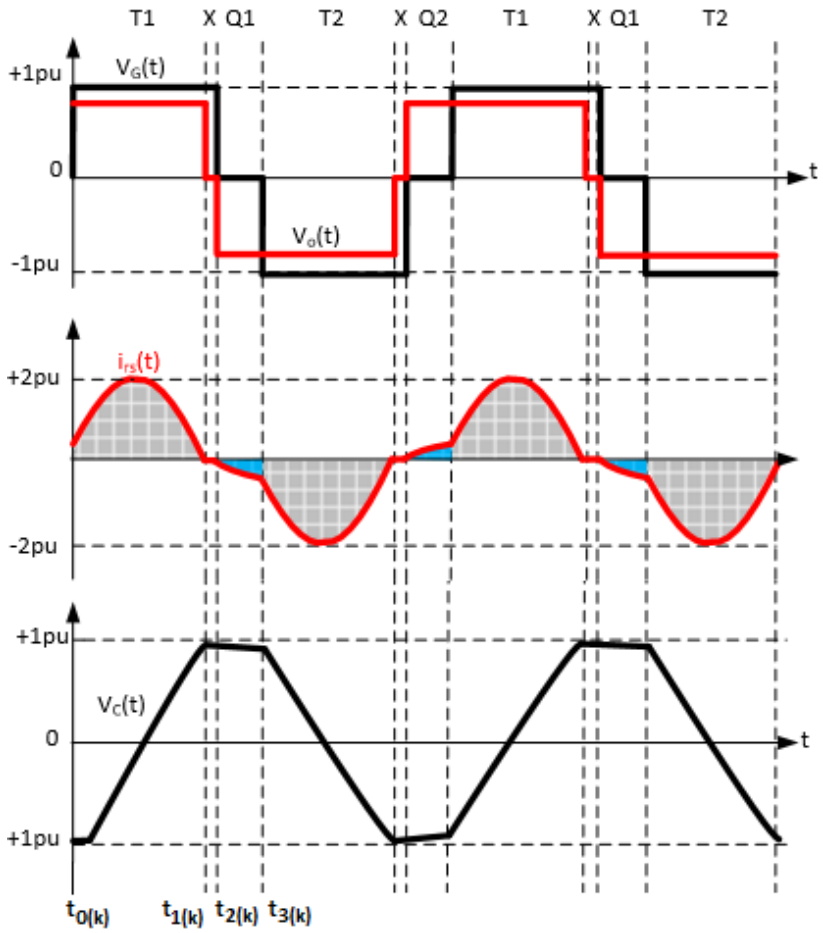

Figure 2.5: Resonant current, Voltage on the turbine side of the transformer and Tank capacitor voltage waveforms. [10]

2.3 Mathematical Model of SRC#

The SRC# is modeled by means of discrete time modeling. This method evaluates the state variables of the considered system only in finite time instants, which represent a border between two different circuit states due to switches and diodes commutations. This way, the relation between the state variables evaluated in two consecutive time instants will be given by the solution of a dynamic linear circuit. The state variables of the SRC# are defined as the resonant current i_r and the capacitor voltage v_{cr}.

For each switching cycle, two *events* k and $k+1$, are distinguished, as shown in Figure 2.5. Moreover, each event is composed by three sub-intervals:

- Event k
  - time interval $t_{0(k)}$ - $t_{1(k)}$, T_1 and T_4 ON, T_1 sub-interval;
  - time interval $t_{1(k)}$ - $t_{2(k)}$, no conduction, X sub-interval;
  - time interval $t_{2(k)}$ - $t_{3(k)}$, D_1 and T_3 ON, Q_1 sub-interval.
- Event $k+1$
  - time interval $t_{0(k+1)}$ - $t_{1(k+1)}$, T_2 and T_3 ON, T_2 sub-interval;
  - time interval $t_{1(k+1)}$ - $t_{2(k+1)}$, no conduction, X sub-interval;
  - time interval $t_{2(k+1)}$ - $t_{3(k+1)}$, D_2 and T_4 ON, Q_2 sub-interval.

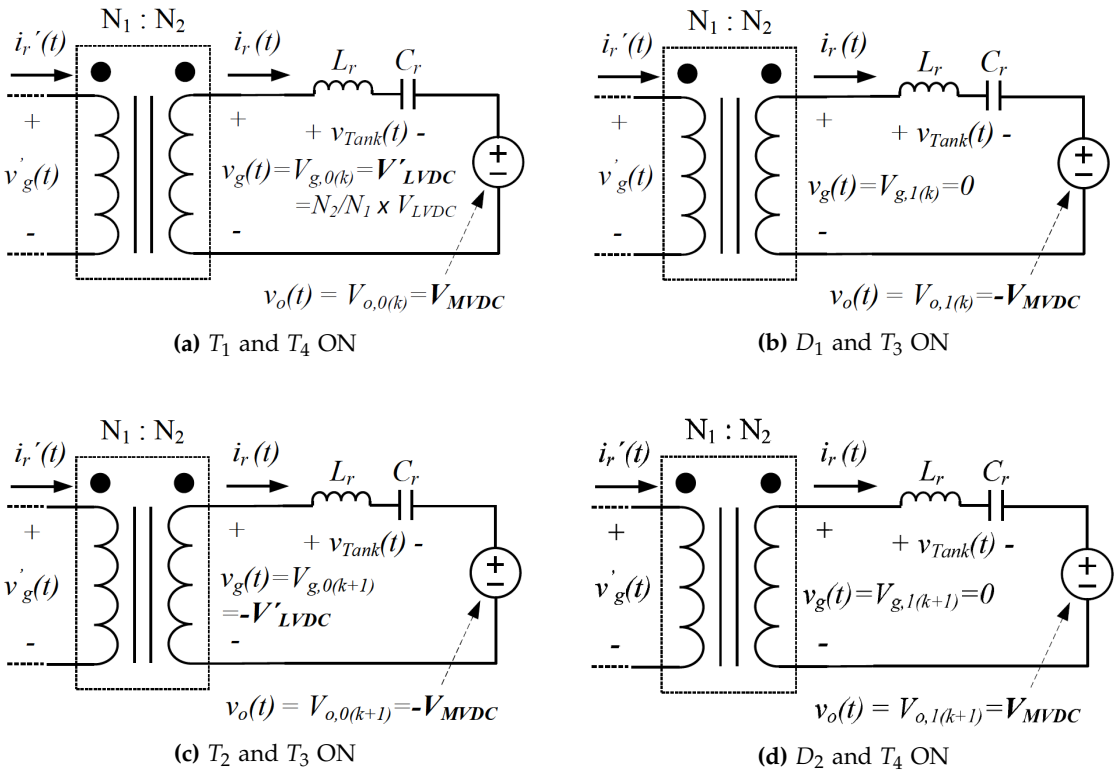

(a) T_1 and T_4 ON

(b) D_1 and T_3 ON

(c) T_2 and T_3 ON

(d) D_2 and T_4 ON

Figure 2.6: Equivalent circuits in different subintervals of the SRC # [10]

As further approximation, the voltage on the grid side and on the turbine side will be considered constant during each event, adopting the so-called small ripple approximation. By the equivalent circuit of Figure 2.6a, representing the first sub-interval of event k, also defined as (T_1, T_4) ON, Equation 2.6 and Equation 2.7 are obtained:

For $t_{0(k)} \leq t \leq t_{1(k)}$ (T_1, T_4 ON)

$$v_g = L_r \frac{di_r}{dt} + v_{cr} + v_o \tag{2.6}$$

$$i_r = C_r \frac{dv_{cr}}{dt} \tag{2.7}$$

By the solution of these dynamic equations, a relationship between the value of the state variables at the time instants $t_0(k)$ and $t_1(k)$ can be provided. During the X sub-interval no variations in the state variables are observed, the voltage across the capacitor is fixed due to the zero tank current. The equivalent circuit for the third sub-interval is finally represented in Figure 2.6b. The initial value of the tank current will be zero, while the initial value of the capacitor voltage is given by the solution of previous Equation 2.6 and Equation 2.7. In this case, Equation 2.7, for the tank current, keeps to be valid, and Equation 2.8 is obtained by inspection of the circuit.

For $t_{2(k)} \leq t \leq t_{3(k)}$ (D_1, T_3 ON)

$$0 = L_r \frac{di_r}{dt} + v_{Cr} - v_o \tag{2.8}$$

Thus, a relation between the values of state variables at the beginning and at the end of each event k is found. The final values of tank current and resonant voltage across capacitor will constitute the initial values for the analysis of next event $k+1$. Likewise, the same analysis could be done for the other three intervals of this event. A discrete-time non linear state space model can now be obtained by a proper choice of two formal state variables:

$$x_{1(k)} = I_{r,0(k)};\ \ x_{1(k+1)} = -I_{r,0(k+1)} \tag{2.9}$$

$$x_{2(k)} = V_{Cr,0(k)};\ \ x_{2(k+1)} = -V_{Cr,0(k+1)} \tag{2.10}$$

The incremental ratio of the state variables over one whole event is now approximated with its limit for an infinitesimal time interval, as it is shown in Equation 2.11.

$$\dot{x}_i(k) = \frac{x_{i(k+1)} - x_{i(k)}}{t_{0(k+1)} - t_{0(k)}} = \frac{2}{T_s} \cdot \left(x_{i(k+1)} - x_{i(k)}\right) \tag{2.11}$$

This last approximation allows to write the continuous time state space model reported in Equation 2.12 and Equation 2.13. Consider that x_1 is representing always the value of the tank current at the beginning of each event, as well as x_2 is the value of the voltage across the capacitor at the same time instant. The detailed analysis leading to this model

is described in the Appendix A.

$$\begin{aligned}\dot{x}_1 =& \frac{2}{T_s} \cdot \Big\{ [sin(\omega_{rs}\beta) \cdot sin(\omega_{rs}\alpha) - 1] \cdot x_1 \\ &+ \frac{1}{Z_r} cos(\omega_{rs}\beta) \cdot sin(\omega_{rs}\alpha) \cdot x_2 \\ &- \left[\frac{2}{Z_r} sin(\omega_{rs}\alpha) - \frac{1}{Z_r} cos(\omega_{rs}\beta) \cdot sin(\omega_{rs}\alpha) \right] \cdot V_o \\ &+ \left[\frac{1}{Z_r} sin(\omega_{rs}\alpha) - \frac{1}{Z_r} cos(\omega_{rs}\beta) \cdot sin(\omega_{rs}\alpha) \right] \cdot V_g \Big\} \\ &= f_1(x_1, x_2, V_g, V_o, f_s)\end{aligned} \tag{2.12}$$

$$\begin{aligned}\dot{x}_2 =& \frac{2}{T_s} \cdot \Big\{ -Z_r \cdot sin(\omega_{rs}\beta) \cdot cos(\omega_{rs}\alpha) \cdot x_1 \\ &- [cos(\omega_{rs}\beta) \cdot cos(\omega_{rs}\alpha) + 1] \cdot x_2 \\ &+ [2cos(\omega_{rs}\alpha) - cos(\omega_{rs}\beta)cos(\omega_{rs}\alpha) - 1] \cdot V_o \\ &+ [-cos(\omega_{rs}\alpha) + cos(\omega_{rs}\beta) \cdot cos(\omega_{rs}\alpha)] \cdot V_g \Big\} \\ &= f_2(x_1, x_2, V_g, V_o, f_s)\end{aligned} \tag{2.13}$$

where:

$$Z_r = \sqrt{\frac{L_r}{C_r}} \tag{2.14}$$

$$\omega_r = \frac{1}{\sqrt{L_r C_r}} \tag{2.15}$$

$$\omega_{rs} = \frac{\omega_r}{\omega_s} = \frac{f_r}{f_s} \tag{2.16}$$

$$tan(\omega_{rs}\beta) = -\frac{Z_r x_1}{V_g - V_o - x_2} \tag{2.17}$$

$$\alpha = \pi - \frac{\pi}{\omega_{rs}} \tag{2.18}$$

Particular attention is needed for Equation 2.17, defining the conduction angle of the IGBTs T_1 and T_4 during event k. This value should be always in the range:

$$0 \leq \beta \leq \frac{\pi}{\omega_{rs}} \tag{2.19}$$

For the output current equation, the following result is obtained considering the output current constant and equal to its mean value during each event:

$$\begin{aligned} i_o = \frac{1}{\pi \cdot \omega_{rs} \cdot Zr} \{ & [sin(\omega_{rs}\beta) \cdot (2 - cos(\omega_{rs}\alpha))] \cdot Z_r \cdot x_1 \\ & + [-1 + 2cos(\omega_{rs}\beta) - cos(\omega_{rs}\beta) \cdot cos(\omega_{rs}\alpha))] \cdot x_2 \\ & + [-3 + 2 \cdot cos(\omega_{rs}\beta) + 2 \cdot cos(\omega_{rs}\alpha) - cos(\omega_{rs}\beta) \cdot cos(\omega_{rs}\alpha)] \cdot V_o \\ & + [2 \cdot (1 - cos(\omega_{rs}\beta)) - cos(\omega_{rs}\alpha) + cos(\omega_{rs}\beta) \cdot cos(\omega_{rs}\alpha)] \cdot V_g \} \\ & = f_o(x_1, x_2, V_g, V_o, f_s) \end{aligned} \tag{2.20}$$

Equations from 2.12 to 2.18 represent the state space model of SRC#. Approximations leading to this model are here recollected:

- effect of magnetizing current absorbed by transformer is neglected;
- Sub-intervals $(D_1, T_3)ON$ and $(D_2, T_4)ON$ do not occur, being replaced by X sub-intervals;
- small ripple approximation: voltages applied on the turbine side and on the grid side are considered as constant during each event as well as the current delivered in the grid side is considered equal to its mean value during each event;

2.4 Steady State Operation

The model developed in the previous section 2.3, and described by state-space Equation 2.12 and Equation 2.18 together with Equation 2.20, is heavily non-linear, and it does not allow to design a controller by means of classical linear control theory. In order to design a proper controller, it is possible to develop a linear model of the converter around each operating condition. Therefore, the purpose of this paragraph is to present a way to find the steady state operating points of the converter.

In steady state, values of input and state variables are fixed. To determine the proper value of state variables corresponding to each set of input variables, there are two possible ways. As first option, time derivatives in Equation 2.12 and Equation 2.13 could be set to zero. The problem ends up being a non linear system of two equations in two variables. As second opportunity, state plane analysis of the converter can be performed, reducing steady state relations between state and input variables to simple geometry.

The converter has only two state variables, the voltage across the resonant capacitor (v_{Cr}) and the tank current flowing through the inductor (i_r). A state plane using v_{Cr} and $Z_r \cdot i_r$ as orthogonal axis can be set, where Z_r is defined in Equation 2.14.

Consider first the sub-interval (T_1, T_4) ON, during the event k. By the solution of equations 2.6-2.7, it results that the system evolution outlines a circular trajectory in the defined state plane, centered in $C_{0(k)}$ and of radius $R_{0(k)}$:

$$C_{0(k)} = (V_{g,0(k)} - V_{o,0(k)}, 0) \tag{2.21}$$

$$R_{0(k)} = \sqrt{\left(V_{g,0(k)} - V_{o,0(k)} - V_{Cr,0(k)}\right)^2 + \left(Z_r \cdot I_{r,0(k)}\right)^2} \tag{2.22}$$

The trajectory is the circumference sector, starting from $(V_{Cr,0(k)}, I_{r,0(k)})$ and crossing the capacitor voltage axis ($i_r = 0$). The angle spanned by this trajectory, seen from the center $C_{0(k)}$ is:

$$\omega_r \cdot (t_{1(k)} - t_{0(k)}) = \omega_{rs} \cdot \beta_k \tag{2.23}$$

An example for the developed study case and steady state conditions is portrayed in Figure 2.7. Here a high voltage difference between the voltages on the two sides of the transformer of the converter is used in order to highlight the trajectory shape.

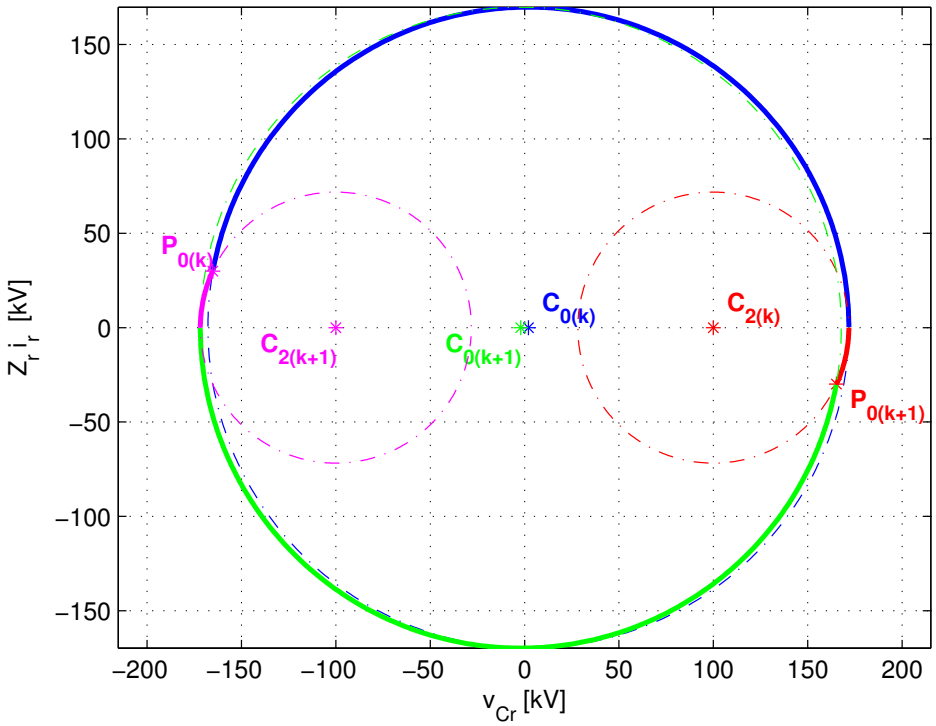

Figure 2.7: Trajectory in the State Space of study case SRC# in Steady State Operation. - $V_g = 4080V$; $V_o = 100kV$; $f_s = 1000Hz$

When the current becomes zero, there is a sub-interval of non-conduction due to the reverse biasing of the diode bridge. During this sub-interval the current keeps being zero, and the resonant capacitor is not being charged or discharged, thus it keeps its voltage value. A new change in state variables occurs in the next sub-interval (D_1, T_3) ON described by equations 2.7-2.8. Solving these last ones, the outlined trajectory in the state plane ends up being again a circumference sector, centered in $C_{2(k)}$ and of radius $R_{2(k)}$:

$$C_{2(k)} = (V_{o,2(k)}, 0) \tag{2.24}$$

$$R_{2(k)} = |V_{o,2(k)} + V_{Cr,2(k)}| \tag{2.25}$$

This circumference sector lasts from the point $(V_{Cr,1(k)}, 0)$ until the point $P_{0(k+1)}$, representing the starting point for the representation of the following $k+1$ event. Spanned angle, respect to the center $C_{2(k)}$ is:

$$\omega_r \cdot (t_{3(k)} - t_{2(k)}) = \omega_{rs} \cdot \alpha_k \tag{2.26}$$

The trajectory in the state plane has to be a closed curve in steady state conditions, as shown in Figure 2.7. The closed shape of the trajectory fix the value of the voltage across the capacitor when the current makes a zero crossing. Consider the triangle ABC, shown in the following Figure 2.8.

The vertices are defined as follows:

$$A = C_{0(k+1)}; \quad B = C_{2(k)}; \quad C = P_{0(k+1)} \tag{2.27}$$

The dimensions of the three sides of the highlighted triangle are defined as:

$$a = |\overline{AB}| = V_g \tag{2.28}$$

$$b = |\overline{BC}| = V_{Cr,1(k)} - V_o \tag{2.29}$$

$$c = |\overline{AC}| = V_{Cr,1(k)} - V_g + V_o \tag{2.30}$$

Moreover, by inspection of the same Figure 2.8:

$$\widehat{CAB} = \pi - \omega_{rs} \cdot \beta \tag{2.31}$$

$$\widehat{ABC} = \pi - \omega_{rs} \cdot \alpha = \pi \cdot (2 - \omega_{rs}) \tag{2.32}$$

$$\widehat{ACB} = \pi - \widehat{CAB} - \widehat{ABC} \tag{2.33}$$

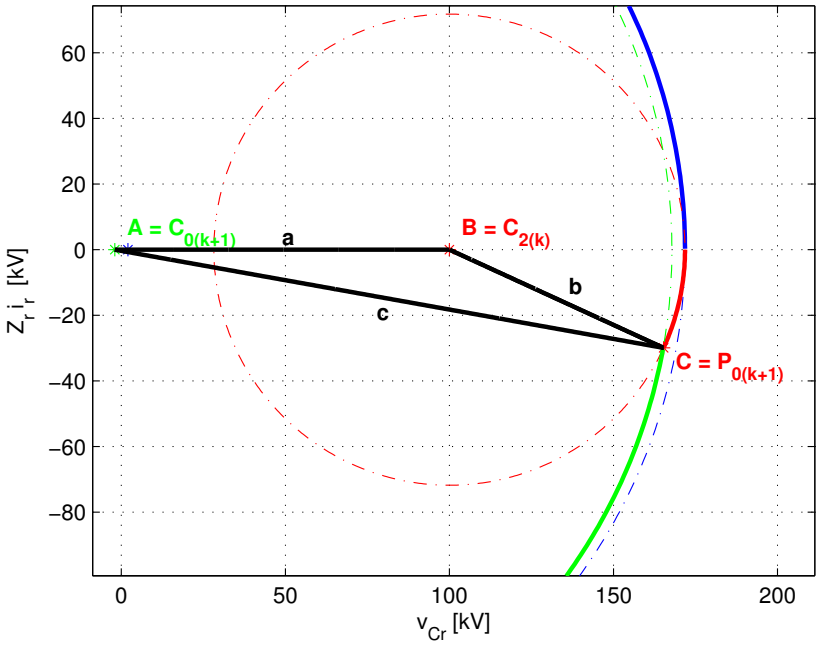

Figure 2.8: Particular of the state space trajectory of SRC#, operating in steady state: $V_g = 4080V$; $V_o = 100kV$; $f_s = 1000Hz$

By Carnot's theorem the voltage across the capacitor when the current approaches zero is a well-known function of the constant input variables:

$$V_{Cr,1(k)} = \frac{V_g \cdot V_o \cdot [1 + cos(2 - \omega_{rs})\pi)]}{2V_o - V_g \cdot [1 - cos((2 - \omega_{rs})\pi)]} \tag{2.34}$$

The output current, due to the effect of the filter that will be present on the grid side, can be approximated by its mean value in each event, as expressed by Equation 2.1. The stored charge in the capacitor in each event is linked to the peak value of the capacitor voltage itself by Equation 2.2. Thus following result is valid:

$$Io = 4C_r V_{Cr,1(k)} f_s \tag{2.35}$$

Trigonometric considerations lead also to the knowledge of $V_{Cr,0(k)}$ and $I_{r,0(k)}$ for fixed input variables:

$$V_{Cr,0(k)} = -(V_o + (V_{Cr,1(k)} - V_o)) \cdot cos(\omega_{rs}\alpha) \tag{2.36}$$

$$I_{r,0(k)} = \frac{(V_{Cr,1(k)} - V_o) sin(\omega_{rs}\alpha)}{Z_r} \tag{2.37}$$

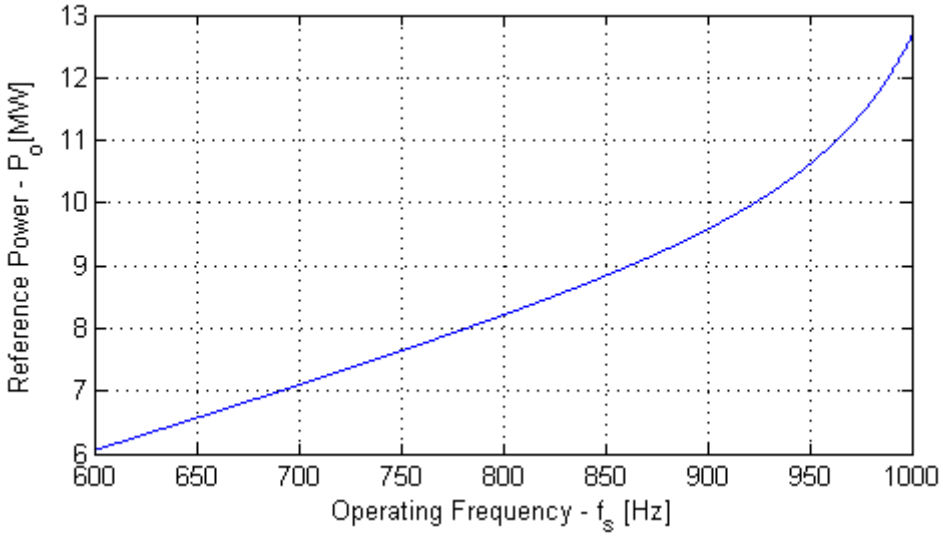

Figure 2.9: Steady state values of output power for the study case converter operated at different switching frequencies and fixed voltages: $V_g = 4040V$, $V_o = 100kV$

Results obtained for different switching frequencies, and fixed values of turbine side and grid side voltages are illustrated for the study case converter in Figure 2.9 and Figure 2.10. By the developed expressions, is possible to find operating points of the converter in the switching frequency range of validity of the model (see Equation 2.5). These relations could also be used in order to build a feedforward control for the converter.

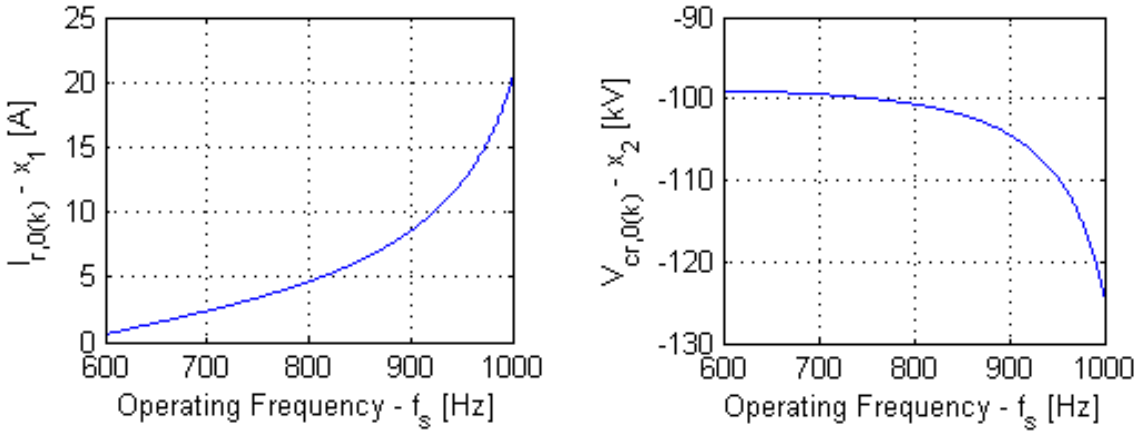

(a) Tank current at the beginning of event k. *(b) Capacitor voltage at the beginning of event k.*

Figure 2.10: Steady state values of state variables for the study case converter, operated at different switching frequencies and fixed voltages: $V_g = 4040V$, $V_o = 100kV$

Chapter 3

Controller Design and Harmonic Model of the SRC#

The model of the SRC# is here linearized around a certain operating condition, obtaining main transfer functions useful for the harmonic susceptibility study and for the design of the controller. The interactions of the converter with the output filter is also examined in detail. As result of the chapter, the behaviour of the converter and the filter, respect to voltage variations in the DC power collection grid, will be described by the means of one transfer function. An harmonic model for the converter is therefore obtained, that is an equivalent admittance for each frequency of the voltage disturbance.

3.1 Small Signal Model of SRC#

A linearized state-space model of the SRC# is obtained for a specific operating condition.

$$\begin{bmatrix} \dot{\tilde{x}}_1 \\ \dot{\tilde{x}}_2 \end{bmatrix} = \underbrace{\begin{bmatrix} \left.\frac{\partial f_1}{\partial x_1}\right|_{OP} & \left.\frac{\partial f_1}{\partial x_2}\right|_{OP} \\ \left.\frac{\partial f_2}{\partial x_1}\right|_{OP} & \left.\frac{\partial f_2}{\partial x_2}\right|_{OP} \end{bmatrix}}_{\mathbf{A}} \begin{bmatrix} \tilde{x}_1 \\ \tilde{x}_2 \end{bmatrix} + \underbrace{\begin{bmatrix} \left.\frac{\partial f_1}{\partial f_s}\right|_{OP} & \left.\frac{\partial f_1}{\partial v_g}\right|_{OP} & \left.\frac{\partial f_1}{\partial v_o}\right|_{OP} \\ \left.\frac{\partial f_2}{\partial f_s}\right|_{OP} & \left.\frac{\partial f_2}{\partial v_g}\right|_{OP} & \left.\frac{\partial f_2}{\partial v_o}\right|_{OP} \end{bmatrix}}_{\mathbf{B}} \begin{bmatrix} \tilde{f}_s \\ \tilde{v}_g \\ \tilde{v}_o \end{bmatrix} \tag{3.1}$$

$$\tilde{i}_o = \underbrace{\begin{bmatrix} \left.\frac{\partial f_o}{\partial x_1}\right|_{OP} & \left.\frac{\partial f_o}{\partial x_2}\right|_{OP} \end{bmatrix}}_{\mathbf{C}} \begin{bmatrix} \tilde{x}_1 \\ \tilde{x}_2 \end{bmatrix} + \underbrace{\begin{bmatrix} \left.\frac{\partial f_o}{\partial f_s}\right|_{OP} & \left.\frac{\partial f_o}{\partial v_g}\right|_{OP} & \left.\frac{\partial f_o}{\partial v_o}\right|_{OP} \end{bmatrix}}_{\mathbf{D}} \begin{bmatrix} \tilde{f}_s \\ \tilde{v}_g \\ \tilde{v}_o \end{bmatrix} \tag{3.2}$$

Input - output transfer functions are defined in Equation 3.3.

$$\tilde{i}_o(s) = \begin{bmatrix} G_1(s) & G_2(s) & G_3(s) \end{bmatrix} \begin{bmatrix} \tilde{f}_s \\ \tilde{v}_g \\ \tilde{v}_o \end{bmatrix} \tag{3.3}$$

where

$$G_1(s) = \left.\frac{\tilde{i}_o(s)}{\tilde{f}_s(s)}\right|_{\tilde{v}_g(s)=0,\tilde{v}_o(s)=0} \quad , G_2(s) = \left.\frac{\tilde{i}_o(s)}{\tilde{v}_g(s)}\right|_{\tilde{f}_s(s)=0,\tilde{v}_o(s)=0} \quad , G_3(s) = \left.\frac{\tilde{i}_o(s)}{\tilde{v}_o(s)}\right|_{\tilde{f}_s(s)=0,\tilde{v}_g(s)=0}$$

A Matlab script has been developed to evaluate the transfer functions defined in Equation 3.3 for different operating conditions.

In Table 3.1 some operating conditions are defined. They differ only for the operating switching frequency and the output power P_o. All the voltages are fixed. The voltage on the turbine side, reflected to the grid side is always higher than the voltage on the grid side allowing a positive power flow from the turbine to the grid. Steady state values of the state variables from the developed model are closed to the values found by PLECS simulations. It is worth noting that also PLECS simulations consider the switches as ideal.

Input Variable		OP_1	OP_2	OP_3
V_g [kV]		4.04	4.04	4.04
V_o [kV]		100	100	100
f_s [Hz]		600	800	1000
P_o [MW]		6.213	8.213	12.67
x_1 [A]	Model	0.5765	4.6325	20.2377
	PLECS	0.568913	4.61398	20.0542
x_2 [kV]	Model	-99.0257	-100.6324	-124.2349
	PLECS	-99.0251	-100.623	-123.895

Table 3.1: Simulation parameters: Input voltage V_g, Output voltage V_o, Output power P_o, tank current at $t_{0(k)}$ (x_1) and tank voltage at $t_{0(k)}$ (x_2).

The zeros and poles for the transfer functions defined in Equation 3.3, evaluated in the operating points illustrated in Table 3.1, are shown in Table 3.2.

3.2 Output Filter Interaction

The current delivered from the converter has a high harmonic content at twice the switching frequency and its multiples, and at the moment only the mean value of the output current in one event has been considered as the real output current. A filter has to be placed on the output side of the converter in order to decrease as much as possible the current harmonics occurring at twice the switching frequency and its multiples. An LC

Table 3.2: Zeros and poles of the transfer function $G_1(s)$,$G_2(s)$, and $G_3(s)$ represented by Equation 3.3 for operating points in Table 3.1. In the last row $G_i(s)$, the common poles of all thetransfer functions are represented.

		OP_1	OP_2	OP_3
G_1	$z_1\ [\frac{rad}{s}]$	-2384	-1622	-2125
	$z_2\ [\frac{rad}{s}]$	-1200	-1422	-707.8
	$Gain[\frac{A}{Hz}]$	$0.616 \cdot 10^{-3}$	$0.010 \cdot 10^{-3}$	$102.0 \cdot 10^{-3}$
G_2	$z_1\ [\frac{rad}{s}]$	-1200	-1815	-3657
	$z_2\ [\frac{rad}{s}]$	-813.7	-1600	-2000
	$Gain[\frac{A}{V}]$	$118.0 \cdot 10^{-3}$	$2.170 \cdot 10^{-3}$	$1.370 \cdot 10^{-3}$
G_3	$z_1\ [\frac{rad}{s}]$	-1200	-1577	-3325
	$z_2\ [\frac{rad}{s}]$	-15.80	-955.5	-2050
	$Gain[\frac{A}{V}]$	$673.0 \cdot 10^{-3}$	$33.60 \cdot 10^{-3}$	$32.60 \cdot 10^{-3}$
G_i	$p_1\ [\frac{rad}{s}]$	-2338	-1600	-2000
	$p_2\ [\frac{rad}{s}]$	-1200	-1181	-118.90

filter is chosen for this purpose, as shown in Figure 3.1. The capacitor is placed directly across the output side of the converter, thus current harmonics can flow through it without flowing through the grid and creating overvoltages on the filter inductance.

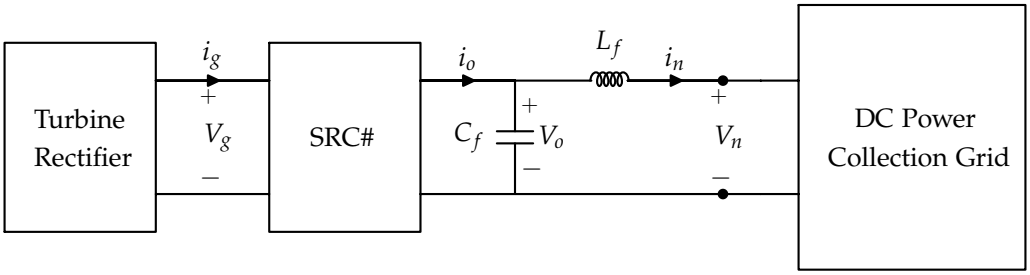

Figure 3.1: Output filter of the SRC#

For the ideal filter of Figure 3.1, the transfer function between the current delivered to the DC network and the output current of the converter is reported in Equation 3.4. The subscript i is meaningful of ideal.

$$G_{fi} = \frac{1}{1 + s^2 \cdot LC} \tag{3.4}$$

By Equation 3.4, the resonant frequency of the filter is defined:

$$f_r = \frac{1}{2\pi\sqrt{L_f C_f}} \tag{3.5}$$

The resonant frequency of the filter has to be set sufficiently smaller than twice the minimum operating frequency of the converter, thus attenuation of current harmonics can be achieved. For the present study case, the resonant frequency of the filter has been set to 100 Hz, six times less than the minimum operating switching frequency. The attenuation of the harmonic content at the fundamental frequency for the lowest operating frequency of 600 Hz is approximately given by Equation 3.6.

$$|G_{fi}(s)|_{s=j2\pi 1200} = 0.7\% \tag{3.6}$$

In order to describe the filter in the most appropriate way, parasitic resistances of filter capacitance and inductance are taken into account. This is also useful to decide value of inductance and capacitance, after their product has already been fixed by the choice of the resonant frequency of the filter.

The modeling of the filter will consider the output current of the converter and the network voltage as input variables, while the current delivered to the grid and the voltage applied to the converter will be the output variables of this linear system. The following four transfer functions, defined by equations 3.7-3.10, are sufficient to completely describe the filter:

$$G_{f1} = \frac{i_n}{i_o} = \frac{\frac{R_C}{R_C+R_L}}{1 + s \cdot \frac{L_f+R_C R_L C_f}{R_C+R_L} + s^2 \cdot \frac{L_f C_f R_c}{R_c+R_L}} \tag{3.7}$$

$$G_{f2} = \frac{v_o}{i_o} = \frac{R_C R_C + R_L(1 + s\frac{L_f}{R_L})}{1 + s \cdot \frac{L_f+R_C R_L C_f}{R_C+R_L} + s^2 \cdot \frac{L_f C_f R_c}{R_c+R_L}} \tag{3.8}$$

$$G_{f3} = \frac{i_n}{v_n} = -\frac{\frac{R_C}{R_C+R_L} \cdot (1 + sR_C C_f)}{1 + s \cdot \frac{L_f+R_C R_L C_f}{R_C+R_L} + s^2 \cdot \frac{L_f C_f R_c}{R_c+R_L}} \tag{3.9}$$

$$G_{f4} = \frac{v_o}{v_g} = \frac{\frac{R_C}{R_C+R_L}}{1 + s \cdot \frac{L_f+R_C * R_L * C_f}{R_C+R_L} + s^2 \cdot \frac{L_f C_f R_c}{R_c+R_L}} \tag{3.10}$$

The interaction of the filter and the converter is described by the block diagram shown in Figure 3.2.

By inspection of the block diagram, the transfer function meaningful of the current delivered to the DC network due to the voltage applied to the filter by the the grid itself is reported in Equation 3.11.

$$G_{OL} = \frac{\tilde{i}_n}{\tilde{v}_n} = G_{f3} + G_{f4} \cdot \frac{G_3}{1 - G_{f2} G_3} \cdot G_{f1} \tag{3.11}$$

For the considered study case, a bode diagram of this transfer function is shown in Figure 3.3, using as parameters the inductance and capacitance values, while their product is fixed to obtain the desired 100 Hz resonant frequency. The higher the inductance

value the lower the harmonic content delivered to the grid. The filter parameters finally adopted are reported in Table 3.3 and will be used to build the controller and implement simulations.

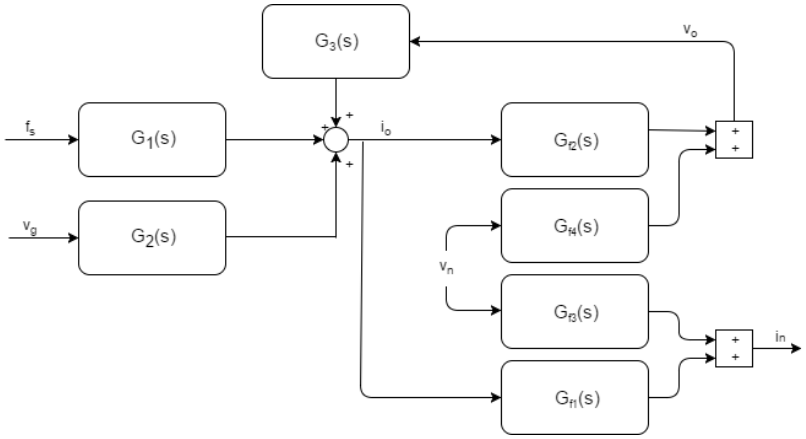

Figure 3.2: Interaction between filter and converter for small perturbations around an operating point.

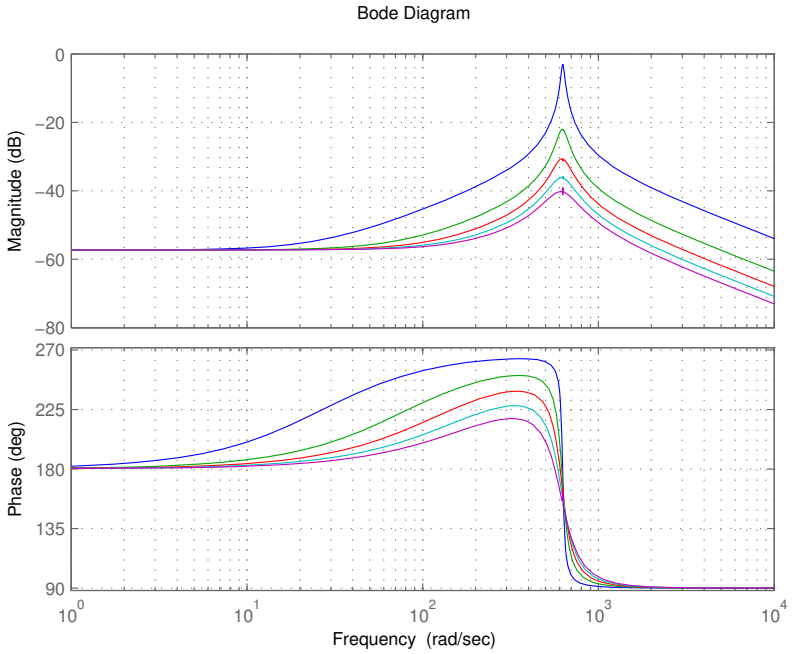

Figure 3.3: Bode diagram of transfer function 3.11 in the developed study case for OP_2, parametric with the filter inductance and capacitance value: (blue line) $L_f = 50\,mH$, $C_f = 50.6\,\mu F$; (green line) $L_f = 150\,mH$, $C_f = 16.9\,\mu F$; (red line) $L_f = 250\,mH$, $C_f = 10.1\,\mu F$; (light blue line) $L_f = 350\,mH$, $C_f = 7.24\,\mu F$; (purple line) $L_f = 450\,mH$, $C_f = 5.63\,\mu F$

Parameter	Value
L_f	$250mH$
C_f	$10\mu F$
R_L	$10m\Omega$
R_C	$100M\Omega$

Table 3.3: Filter parameters for the study case.

Finally, the current delivered to the grid is related with the switching frequency of the converter by the transfer function $H(s)$, defined in Equation 3.12, for each operating point.

$$H(s) = \frac{i_n}{f_s} = \frac{G_1 \cdot G_{f1}}{1 - G_{f2} \cdot G_3} \tag{3.12}$$

3.3 Validation of the Model

The open loop step responses given from the derived transfer functions are compared with the results found by PLECS simulations.

Dynamic simulations of linear model are in good according with PLECS switching model, as illustrated in Figure 3.4, Figure 3.5 and Figure 3.6.

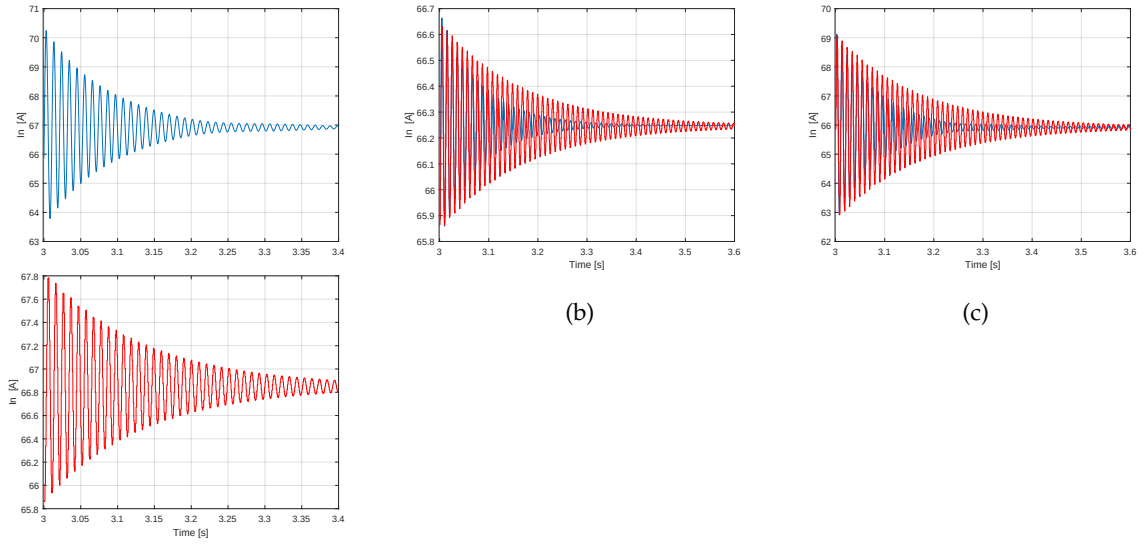

(a) (b) (c)

Figure 3.4: 650 Hz - Open Loop response of i_n from a: (a) 1 A positive step of $i_{n,REF}$. (b) 0.5% negative step of V_g. (c) 0.5% negative step of V_o. Matlab (blue line), Plecs (red line)

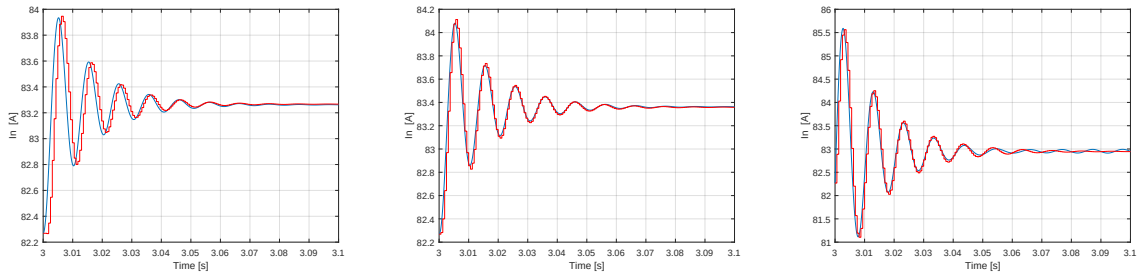

(a) (b) (c)

Figure 3.5: 800 Hz - Open Loop response of i_n from a: (a) 1 A positive step of $i_{n,REF}$. (b) 0.5% negative step of V_g. (c) 0.5% negative step of V_o. Matlab (blue line), Plecs (red line)

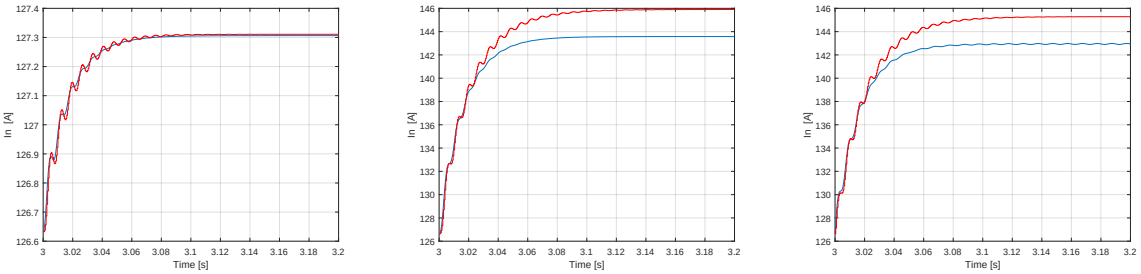

(a) (b) (c)

Figure 3.6: 1000 Hz - Open Loop response of i_n from a: (a) 1 A positive step of $i_{n,REF}$. (b) 0.5% negative step of V_g. (c) 0.5% negative step of V_o. Matlab (blue line), Plecs (red line)

Regarding the transient responses at OP_1 and OP_2, the presence of overshoot and ringing is due to the LC filter at the output of the converter. In particular, the filter gives its influence by adding on the open loop transfer function $H(s)$ two imaginary poles, responsible for overshoot and oscillatory dynamics.

It is also worth to mention that the open loop responses of the converter at OP_3 are not presenting any overshoot and ringing, as present for the other operating points.

The reason behind this behavior at OP_3 is related with the non perfect cancellation of the zeros with the poles of $H(s)$. In order to understand which poles and zeros in $H(s)$ are governing the dynamics, the root locus of the open loop transfer function $H(s)$ at OP_3 is plotted in Figure 3.7.

The presence of the fast zero at $-707.8\frac{rad}{s}$, which is further away to the imaginary axis, it has a negligible impact on dynamics. On the other hand, it can be seen from Figure 3.7 that the real negative pole close to the imaginary axis is a slow pole (dominant) and so, it has a slow decay due to the small real part. This dominant pole at around $-61.2\frac{rad}{s}$, being slower than the double imaginary poles, determines the dynamics of the system in a such way that the influence of the double imaginary poles is negligible. The transient behaviour

of the converter at OP_3, similar to a first order system, is therefore explained.

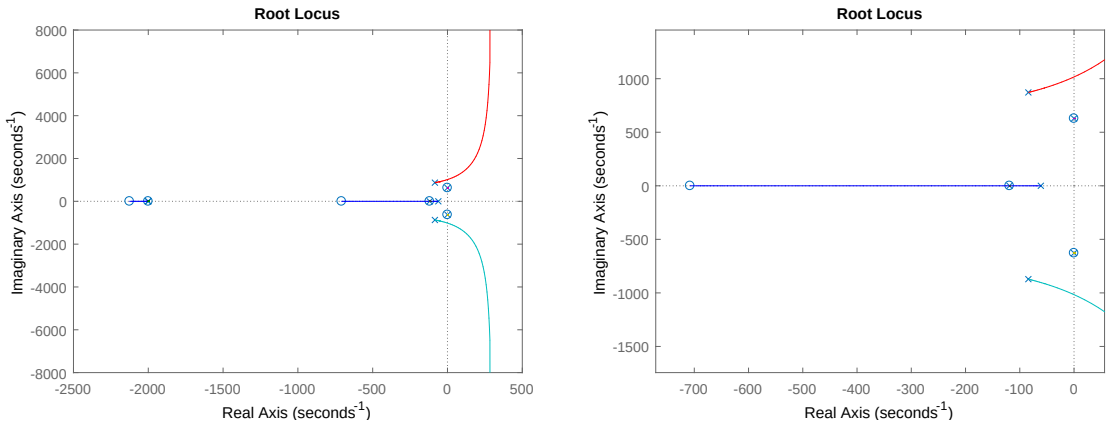

(a) (b)

Figure 3.7: (a) Root locus of $H(s)$ at $1000Hz$. (b) Zoom close to the origin of the Root Locus of $H(s)$ at $1000Hz$.

3.4 Controller Design

A suitable controller to combine with the SRC# is designed to obtain a proper current control loop, illustrated in Figure 3.8.

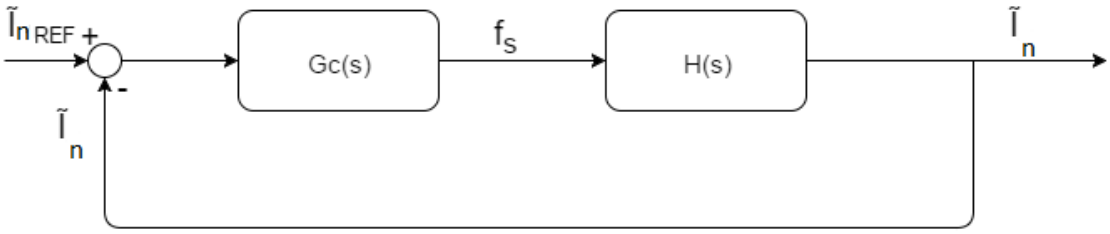

Figure 3.8: Closed loop control system of the small-signal model of SRC#

[5] Main specifications for the design of the controller are here defined:

- *Stability*: the closed loop system has to be asymptotically stable. The Bode stability criterion is used to verify system stability starting from the open loop transfer function $G_c \cdot H$;
- *Zero steady state error*: the output current should reach its reference value once the transient is finished;
- *Settling time*: the control system has fast in order the output to reach the desired

value as soon as possible. Control action finitness imposes an upper limit on the control system settling time;

- *Overshoot and ringing*: these two inconveniences have to be limited. In order to limit them, the phase margin φ_m must be sufficiently large;
- *Disturbances rejection*: the control system forces the process variable back toward the desired setpoint whenever a disturbance on the process causes a deviation.

In the considered study case, the converter transfer functions $G_1(s)$, $G_2(s)$ and $G_3(s)$, defined in Equation 3.3, have been already presented in Table 3.2 for the three operating points defined in Table 3.1. The output LC filter transfer functions have also been defined in Equations 3.7-3.10. As mentioned in the previous section, the block diagram in Figure 3.2 expresses the interactions between filter and converter variables. The open loop transfer function is therefore:

$$T(s) = G_c(s) \cdot H(s) \tag{3.13}$$

The design of the controller G_c starts by studying the frequency response of $H(s)$ for each OP, as plotted in Figure 3.9. It can be seen that around 100 Hz, the resonant frequency of the output LC filter, a peak on the magnitude occurs.

Parasitic resistances of the capacitor C_f and inductor L_f attenuate to finite values the magnitude of the filter transfer functions at the resonant frequency, providing some damping.

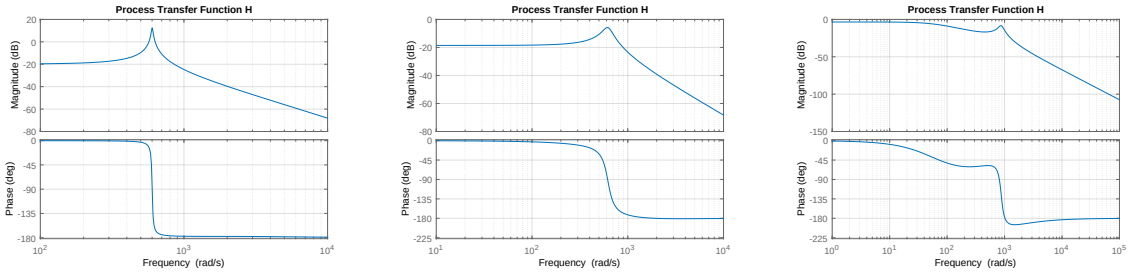

(a) (b) (c)

Figure 3.9: Bode plot of the transfer function $H(s)$ at: (a) OP_1 (b) OP_2 (c) OP_3

Following the specifications mentioned at the beginning of the section, the design of the controller starts by adding an integrator in order not to have steady state error with a step input. Thus, the output current will reach the reference value when the transient is finished.

Second, a pole around the resonant frequency of the output LC filter is added to lower the resonant magnitude peak influence of the filter.

Finally, a gain K is necessary to set a proper crossover frequency f_c which is always lower than the resonant frequency of the output filter; otherwise, the resonant peak will be present in the feedback loop and the phase margin of the open loop transfer function $H(s)$ will be less than 0°, leading to the instability of the closed loop system.

The generic transfer function of the desgined controller G_c is therefore:

$$G_c = \frac{K}{s \cdot (1 - \frac{s}{\omega_p})} \tag{3.14}$$

where

- K: gain of the controller $[\frac{Hz}{A}]$;
- ω_p: pole close to the resonant frequency of the output LC filter $[\frac{rad}{s}]$;

As shown in Figure 3.9, the frequency responses of $H(s)$ differ for each operating point so, the controller design changes for every operating point.

The values of the gain K and the poles of the three controllers implemented for OP_1, OP_2 and OP_3 are:

Table 3.4: Controller parameters for OP_1, OP_2 and OP_3

Operating Point	K [dB]	ω_p $[\frac{rad}{s}]$
OP_1	56.0	-60
OP_2	58.6	-400
OP_3	50.8	-250

An exception has to be considered at OP_3 because, as shown in Figure 3.9(c), the transfer function $H(s)$ presents a pole at low frequencies, around $-61.2\frac{rad}{s}$. This pole is not deleted by any other zero in the open loop transfer function $H(s)$, as it happens for the other operating points where all the poles and the zeros of $H(s)$ were deleting each other.

For OP_3, a zero needs to be added at the controller in order to delete the influence of the pole in $H(s)$ so, the transfer function for the controller $G_c(s)$ at OP_3 is:

$$G_c = K \cdot \frac{(1 - \frac{s}{\omega_z})}{s \cdot (1 - \frac{s}{\omega_p})} \tag{3.15}$$

where ω_z is equal to the low frequenncy pole in $H(s)$, around $-61\frac{rad}{s}$.

The frequency response of open loop transfer functions of the control system are illustrated in Figure 3.10.

It can be seen from Figure 3.10 and Table 3.5 that the angular crossover frequencies of the compensated transfer functions $T(s)$ are different for each operating point.

In order to improve the transient response of the system and to reject harmonic disturbances, the angular crossover frequency ω_c of $H(s)$ should be as high as possible. The

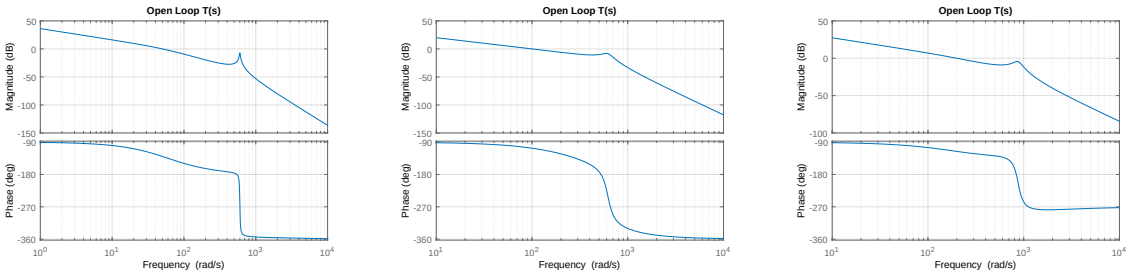

(a) (b) (c)

Figure 3.10: Bode plot of the compensated transfer function $T(s)$ at: (a) OP_1 (b) OP_2 (c) OP_3

Table 3.5: Angular crossover frequency ω_c of $T(s)$ for OP_1, OP_2 and OP_3

Operating Point	ω_c $[\frac{rad}{s}]$
OP_1	50
OP_2	100
OP_3	200

selected crossover frequencies f_c for all the operating points, shown in Table 3.5, are always less than 10% of the switching frequency f_s ($f_c < 0.1 f_s$) in order to not amplify the switching harmonics. [5]

Unfortunately, PLECS simulations show that is not possible to higher the crossover frequency ω_c above a threshold value, different for each OP. If this value is overreached, PLECS simulations and the developed model in MATLAB show increasing differences, as the crossover frequency raises, until stability is lost in PLECS simulations. An output filter with a resonant frequency of $250Hz$ has been considered, in order not to limit the crossover frequency of the control system, due to stability issues. In Figure 3.11 is illustrated that an increase in the crossover frequency raises the difference between the small signal model in MATLAB and the switching model in PLECS.This mismatch comes from the discretization of the controller, done at the end of each event, thus with a variable sampling time always about:

$$T_{sampling} = \frac{1}{2 f_{sw}} \tag{3.16}$$

The crossover frequency of the open loop transfer function $H(s)$, which can be assumed equal to the bandwidth of the system, characterizes the rapidity of the feedback system. Higher the crossover frequency, faster the response of the system.[11]If the system is too fast, the discretization of the controller cannot represent the foreseen dynamics of the control system.

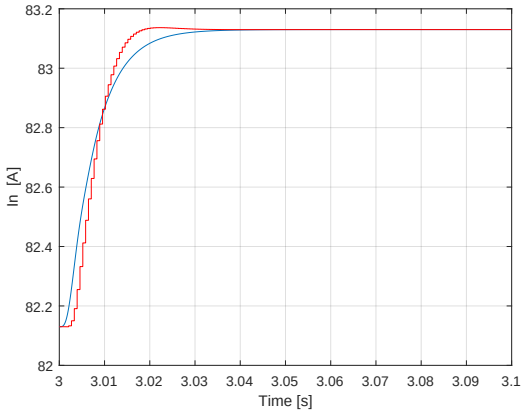

20 Hz of crossover frequency

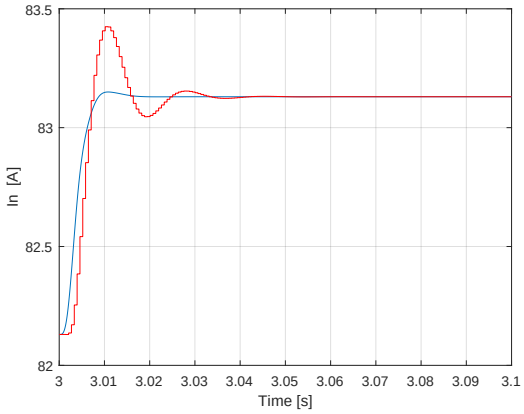

40 Hz of crossover frequency

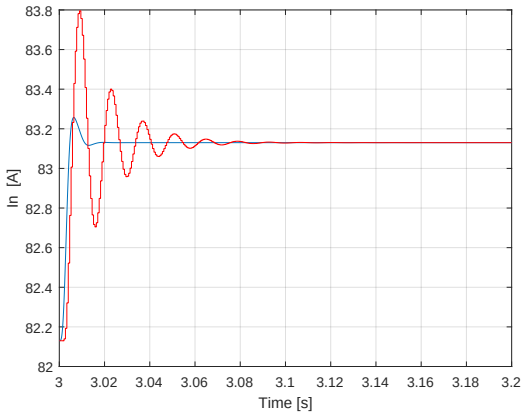

60 Hz of crossover frequency

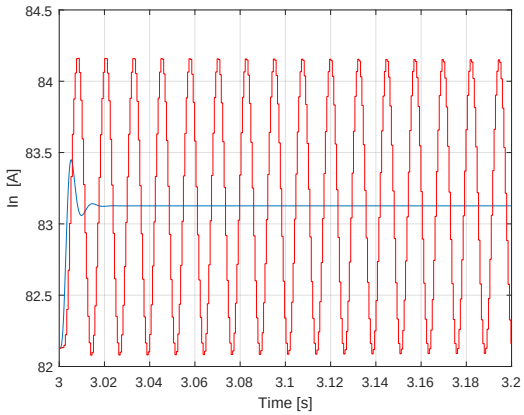

80 Hz of crossover frequency

Figure 3.11: 800 Hz - Closed Loop responses of i_n to 1 A positive step of $i_{n,REF}$ for different crossover frequencies of $H(s)$. Matlab (blue line), Plecs (red line).

The discretization of the controller $G_c(s)$ has been made with Tustin or bilinear approximation which yields the best frequency-domain match between the continuous-time and discretized systems.

Another problem found during the design of the controller is that is not possible to delete the two complex conjugate poles of $H(s)$, leading to resonant dynamics. A controller designed to delete these poles cannot be succesfully implemented in the switching model of the converter. The frequency response of such a kind of controller to a current reference step in MATLAB presents an initial overshoot that lasts less than the sampling time, 0.625 ms (see Figure 3.12). In the switching model it is not possible to represent dynamics lasting less than the sampling period.

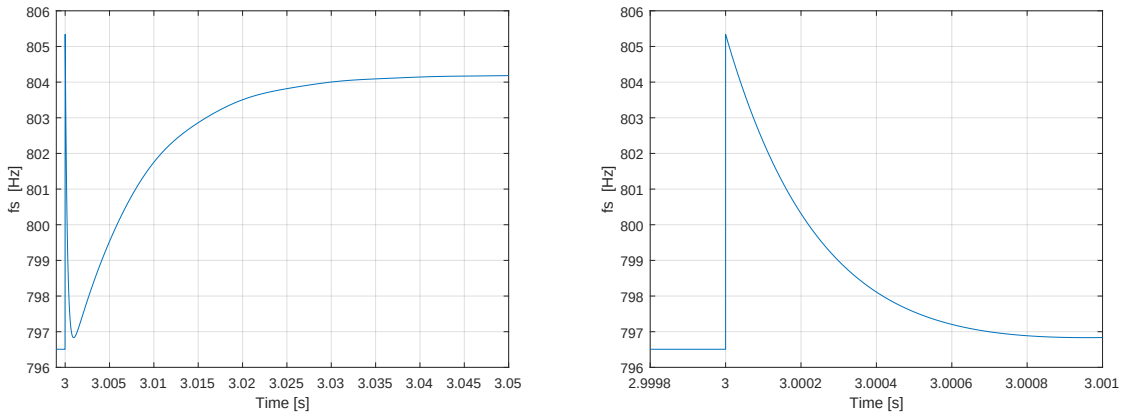

(a) (b)

Figure 3.12: (a) Frequency response of the controller designed to cancel the double imaginary poles of $H(s)$. 1 A positive step change of $i_{n,REF}$. (b) Zoomed view of figure (a) around 3 seconds.

3.5 Validation of the Controller

In order to validate the implementation of the controller in the switching model, the dynamic responses of the closed loop control system for the continuous state-space model and the relative switching model are illustrated together in the following figures.

All the red and blue curves illustrated in Figure 3.13, Figure 3.14 and Figure 3.15 match each others. This means that the state-space model of the controller is well implemented in the switching model.

From the dynamic responses of the closed loop during a step on the reference current $I_{n,REF}$, illustrated in Figure 3.13(a),Figure 3.14(a) and Figure 3.15(a), it can be seen that the settling time between OP_1, OP_2 and OP_3 is different because the crossover frequency chosen for each OP changes. The lower the crossover frequency, the slower the dynamic response.

Another consideration is that the controller is working as expected in response to step disturbances, keeping constant the output current i_n when step changes on the input V_g and output V_o voltages occur.

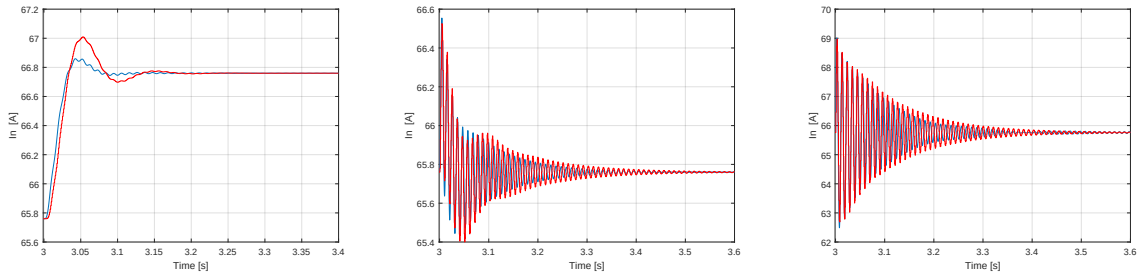

(a) (b) (c)

Figure 3.13: 650 Hz - Closed Loop response of i_n from a: (a) 1 A positive step of $i_{n,REF}$. (b) 0.5% negative step of V_g. (c) 0.5% negative step of V_o. Matlab (blue line), Plecs (red line)

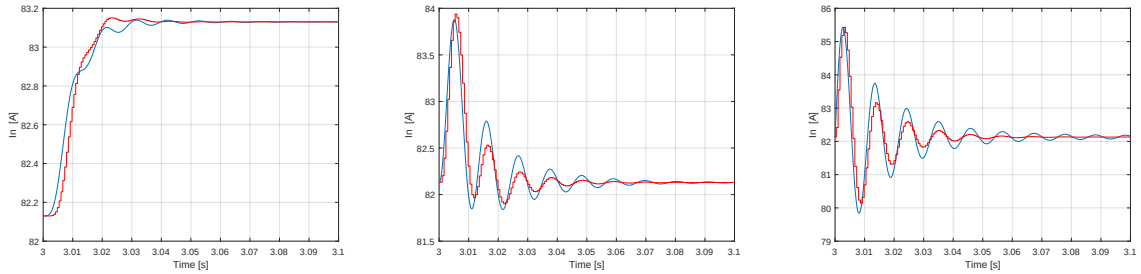

(a) (b) (c)

Figure 3.14: 800 Hz - Closed Loop response of i_n from a: (a) 1 A positive step of $i_{n,REF}$. (b) 0.5% negative step of V_g. (c) 0.5% negative step of V_o. Matlab (blue line), Plecs (red line)

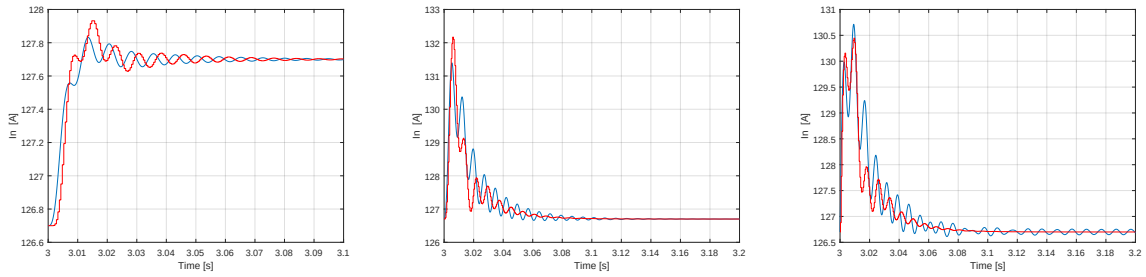

(a) (b) (c)

Figure 3.15: 1000 Hz - Closed Loop response of i_n from a: (a) 1 A positive step of $i_{n,REF}$. (b) 0.5% negative step of V_g. (c) 0.5% negative step of V_o. Matlab (blue line), Plecs (red line)

3.6 Admittance Equivalent Circuit

Consider the SRC# working around one operating point. Assuming that there are no perturbations in the power reference $\tilde{P}_{REF} = 0$ ($\tilde{I}_n = 0$), and in the low voltage DC network $\tilde{V}_g = 0$, the converter can be modelled as an admittance with variable values depending on the frequency of the disturbance. An admittance equivalent circuit is a representation of the converter working around a certain operating point, at a specific frequency of the disturbance $\tilde{V}_n$. It is developed in order to study the current in the grid due to voltage harmonics produced by the MVDC substation.

For the system working in open loop, according to the block diagram in Figure 3.2, the relation between $\tilde{I}_n$ and $\tilde{V}_n$ is given by Equation 3.11. In order to interpret this transfer function as an admittance, a negative sign is added as a convention sign (see Figure 3.16).

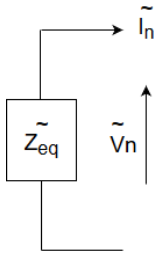

Figure 3.16: Harmonic equivalent of the SRC#

The equation for the closed loop block diagram is given in Equation 3.17. In this case, the block diagram is illustrated in Figure 3.17 and consequently the equation is different due to the implementation of the controller G_c :

$$\tilde{Y}_{EqCL} = \frac{-\tilde{I}_n}{\tilde{V}_n} = -\frac{G_{f3}(s) + \frac{G_{f1}(s)\cdot G_3(s)\cdot G_{f4}(s)}{1-G_3(s)\cdot G_{f2}(s)}}{1 + \frac{G_{f1}(s)\cdot G_1(s)\cdot G_c(s)}{1-G_3(s)\cdot G_{f2}(s)}} \tag{3.17}$$

For each disturbance frequency, the equivalent admittance could be evaluated and represented as a simple RL or RC series branch.

3.7 Equivalent Model for Open Loop

A comparison between the admittance equivalent and the switching model of the converter is made to give a proof of accuracy. As the admittance equivalent has to behave similarly to the switching model, the output current magnitude and phase have to be similar in both cases to avoid any errors in future analysis. A range of harmonic frequencies between 20 Hz and 300 Hz at 500 V amplitude are tested to observe the behaviour of the output current ripple.

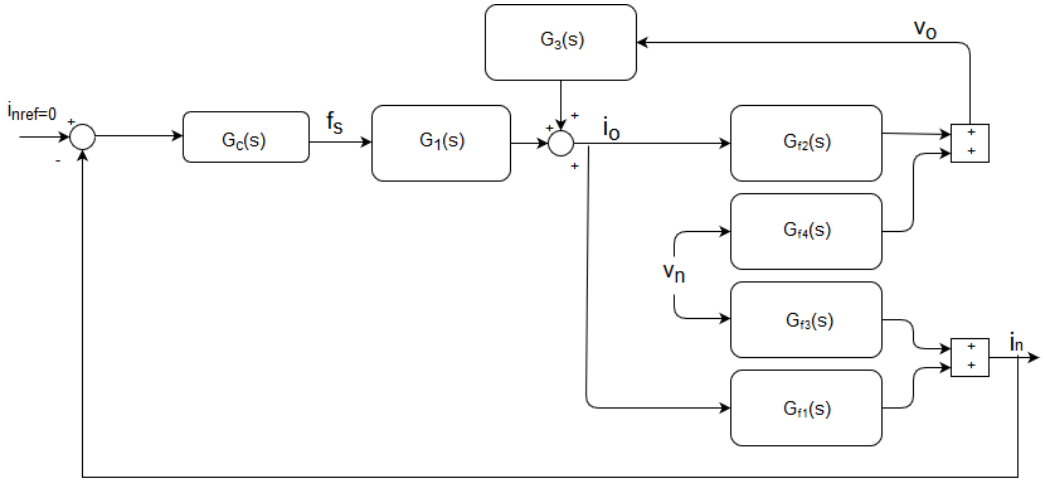

Figure 3.17: Block diagram for Closed Loop

Using Equation 3.11 and previous considerations, the equivalent admittance for the study case converter is developed for the operating points defined in Table 3.1. In figures 3.18-3.20, the network current magnitude and phase is shown, in response to a 500V voltage disturbance in the grid. The behaviour of the converter changes from inductive to capacitive at the resonant frequency of the filter. Both the switching model and the admittance equivalent results are reported to have a comparison. There is a significant difference between the admittance equivalent and switching model at 100 Hz, because of the resonant frequency of the filter. However, for the rest of disturbances the admittance equivalent behaves similarly to the switching model both for amplitude and phase. As it can be seen in Figure 3.18 and Figure 3.19, the fundamental current amplitude is maximum at the resonant frequency of the filter, while it decreases at low or high frequencies. For OP_3, depicted in Figure 3.20, it can be seen that the current has a peak also at 140Hz. This particular behaviour is described by the admittance equivalent transfer function.

As a proof of accuracy, in Table 3.6 is reported the error between the current amplitudes at OP_2 both for the switching model and the admittance equivalent. The error is low as disturbance is far from the resonant frequency of the filter.

Table 3.6: Comparison of diturbance current amplitude for equivalent and switching model working in OP_2, open loop

f_h	20	40	60	80	100	120	140	160	180	200
$\tilde{I}_{eq}$ [A]	0.982	1.744	3.195	6.896	inf	7.178	4.327	3.135	2.485	2.074
$\tilde{I}_{sw}$ [A]	0.960	1.698	3.084	6.013	9.418	7.644	4.497	3.224	2.542	2.115
$Error$ [%]	2.24	2.64	3.47	12.80	inf	6.49	3.92	2.83	2.29	1.97

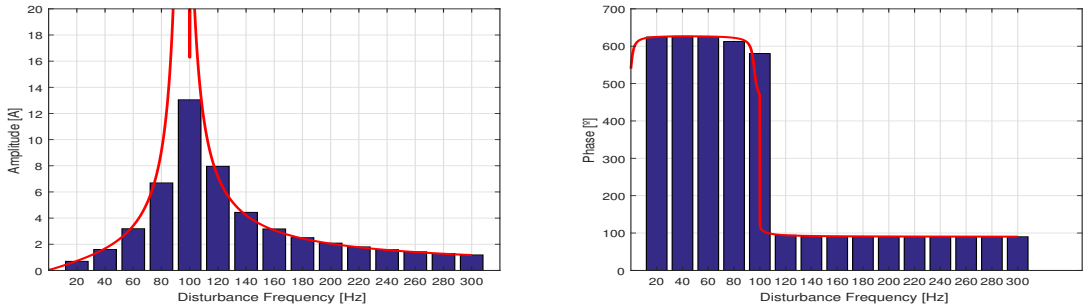

(a) (b)

Figure 3.18: Comparison in open loop between the switching model (blue bar) and the admittance equivalent (red line) at OP_1, harmonic current $\tilde{i}_n$ for a 500 V disturbance at different frequencies: (a) Magnitude (b) Phase between current and disturbance voltage

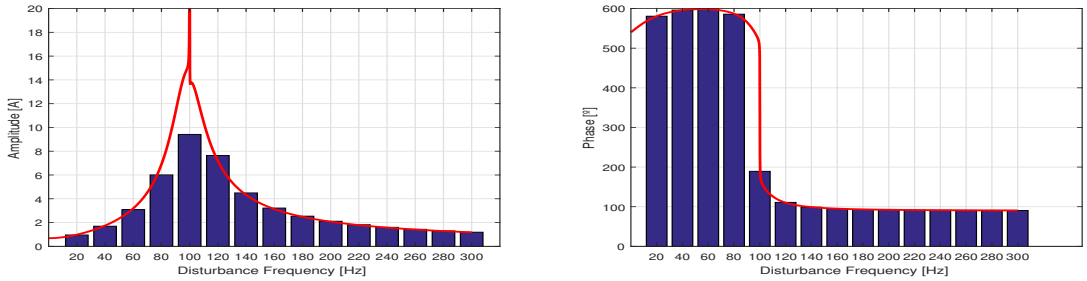

(a) (b)

Figure 3.19: Comparison in open loop between the switching model (blue bar) and the admittance equivalent (red line) at OP_2, harmonic current $\tilde{i}_n$ for a 500 V disturbance at different frequencies: (a) Magnitude (b) Phase between current and disturbance voltage

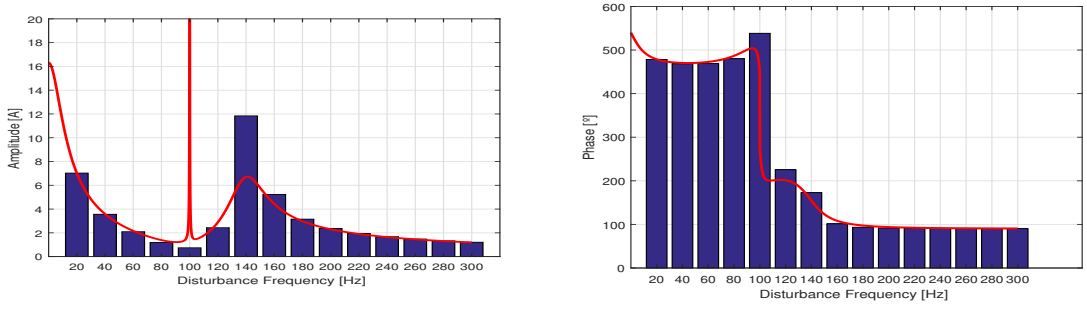

(a) (b)

Figure 3.20: Comparison in open loop between the switching model (blue bar) and the admittance equivalent (red line) at OP_3, harmonic current $\tilde{i}_n$ for a 500 V disturbance at different frequencies: (a) Magnitude (b) Phase between current and disturbance voltage

3.8 Equivalent Model for Closed Loop

In this case, a comparison between the admittance equivalent and switching model with the controller is made. When a controller is introduced to the system, complexity of the equivalent model increases and so does the error between both models. As in the previous section, the fundamental current harmonics for grid voltage disturbances of 500V and different frequencies are reported for the three different operating conditions of Table 3.1, see Figures 3.21-3.23. In order to obtain the admittance equivalent transfer function for different disturbances Equation 3.17 is used. As for the open loop case, at the two operating points OP_1 and OP_2 maximum harmonic current amplitude occurs at the above-mentioned resonant frequency of the filter (see Figure 3.21 and Figure 3.22).
Furthermore, magnitudes are slightly higher than in open loop, since the crossover frequency of the controller is lower than 20 Hz. An important observation can be made for OP_3 ($f_s = 1000Hz$). The open loop current harmonics are high at low frequencies (see Figure 3.20), while the controller is attenuating the current amplitude value until the crossover frequency of 35 Hz (see Figure 3.23).

In Table 3.7, it is reported the error between the switching model and the admittance equivalent for OP_2 ($f_s = 800Hz$) in closed loop.

Difference between the admittance equivalent and switching model, regarding different disturbances, is due to two reasons:

- the implementation of the controller in PLECS leads to a slight variation of the switching frequency when a disturbance is applied, while the equivalent admittance transfer functions are made for a fixed switching frequency.
- around the resonant frequency of the filter high oscillations of the current cause the loss of linear approximations.

Table 3.7: Comparison of disturbance current amplitude for equivalent and switching model working in OP_2, closed loop

f_h	20	40	60	80	100	120	140	160	180	200
$\tilde{I}_{eq}$ [A]	0.954	2.173	4.180	9.983	inf	6.716	4.184	3.078	2.458	2.059
$\tilde{I}_{sw}$ [A]	1.062	2.478	4.360	7.093	9.606	6.863	4.339	3.184	2.531	2.114
$Error$ [%]	10.16	14.03	4.31	28.90	inf	2.14	3.44	3.32	2.88	2.60

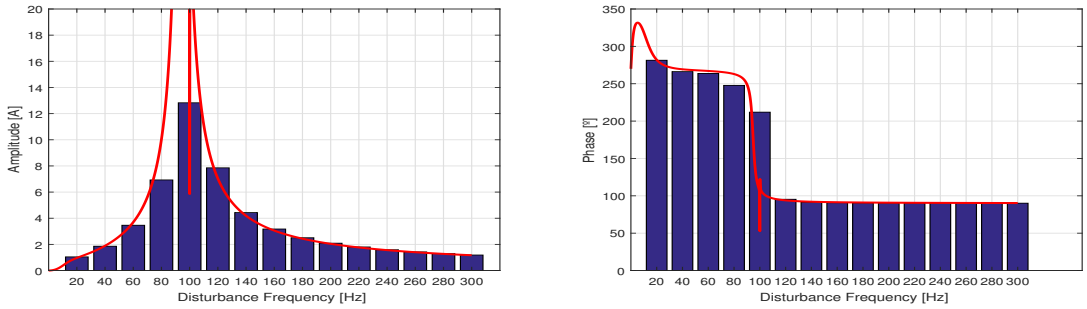

(a) (b)

Figure 3.21: Comparison in closed loop between the switching model (blue bar) and the admittance equivalent (red line) at OP_1, harmonic current $\tilde{i}_n$ for a 500 V disturbance at different frequencies: (a) Magnitude (b) Phase between current and disturbance voltage

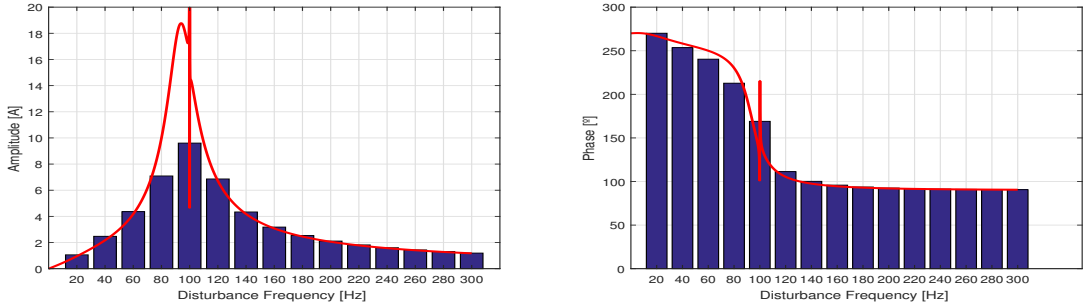

(a) (b)

Figure 3.22: Comparison in closed loop between the switching model (blue bar) and the admittance equivalent (red line) at OP_2, harmonic current $\tilde{i}_n$ for a 500 V disturbance at different frequencies: (a) Magnitude (b) Phase between current and disturbance voltage

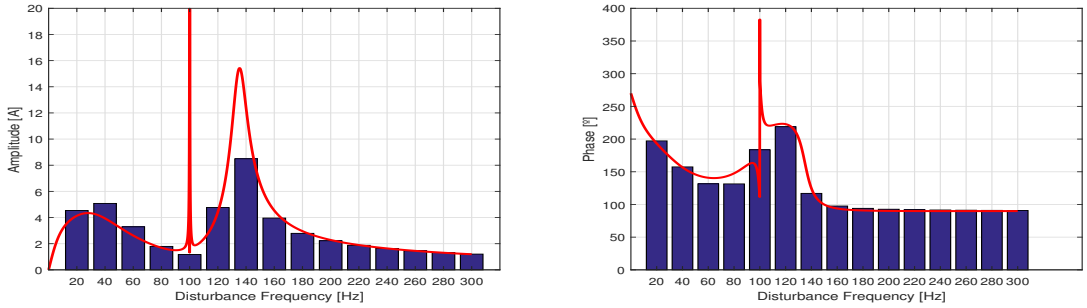

(a) (b)

Figure 3.23: Comparison in closed loop between the switching model (blue bar) and the admittance equivalent (red line) at OP_3, harmonic current $\tilde{i}_n$ for a 500 V disturbance at different frequencies: (a) Magnitude (b) Phase between current and disturbance voltage

Chapter 4

Harmonic Susceptibility Study for DC Collection Grid

In the present chapter, the DC offshore wind farm introduced in section 1.1 is object of an harmonic susceptibility study. For the sake of simplicity, all the wind turbines will be considered operating in similar conditions. The aim of the chapter is therefore to investigate the accuracy of the harmonic model of the SRC#, in order to predict the harmonic currents through the cables of the DC power collection grid. Therefore, the basics of cable modeling are presented in section 4.1, as necessary step for the network simulation. The harmonic susceptibility study setting is firstly described in section 4.2. A frequency scan approach is used to simulate the accurate model of the network, as explained in detail later. The harmonic susceptibility study of the network is then performed in section 4.3, and results obtained with the developed harmonic model are compared with the accurate switching model.

4.1 Cables Model

The models adopted for the submarine cables depend on the application area. For the harmonic studies, *Cigre* recommendation [3] is to use at least a Π section model, varying the parameters of the Π model with the frequency of interest. For submarine cables, due to the skin effect and the eddy currents in the screen and the armour, the variation of the per-length resistance and inductance is a major factor. *Cigre*'s advice can be used for the harmonic susceptibility study only for the developed harmonic model of the SRC#. An accurate harmonic susceptibility study has to consider a more sophisticated model in order to match the real behaviour of the cables for a wider range of frequencies. The most accurate frequency dependent model is too costly from a computational point of view, requiring a large time of simulation. In order to properly simulate the cable behaviour in the frequency range $[0 - 10kHz]$, a rational approximation of the longitudinal admittance by vector fitting is here performed, as suggested in [2], and by the theoretical means

provided in [6].

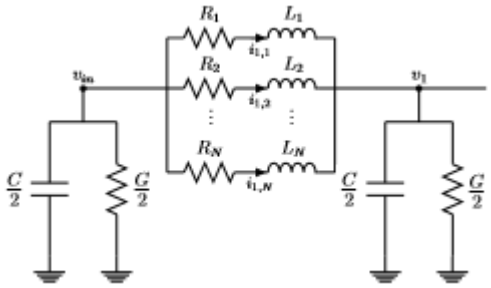

Figure 4.1: Equivalent Π model for the cables. Longitudinal admittance is made up of n parallel branches to take into account its frequency behaviour [2].

The values of the longitudinal admittance, and the shunt capacitance are difficult to derive starting from the geometric parameters, requiring the solution of complex electromagnetic problems. PSCAD software can be usefully employed to overcome this problem. The values of resistance, inductance and capacitance to use at each frequency are calculated by the software itself. From PSCAD data, the capacitance is not varying within the frequency range of interest. Instead, as the frequency rises, the resistance keep increasing, due to the skin effect, and the inductance decreases its value due to the eddy currents in the outer conductors. For the considered study case, eight RL series branches are used to approximate the longitudinal impedance. The frequency dependent behaviour of the cables is described properly in the frequency range of interest, as shown in Figure 4.2 for cable 2.

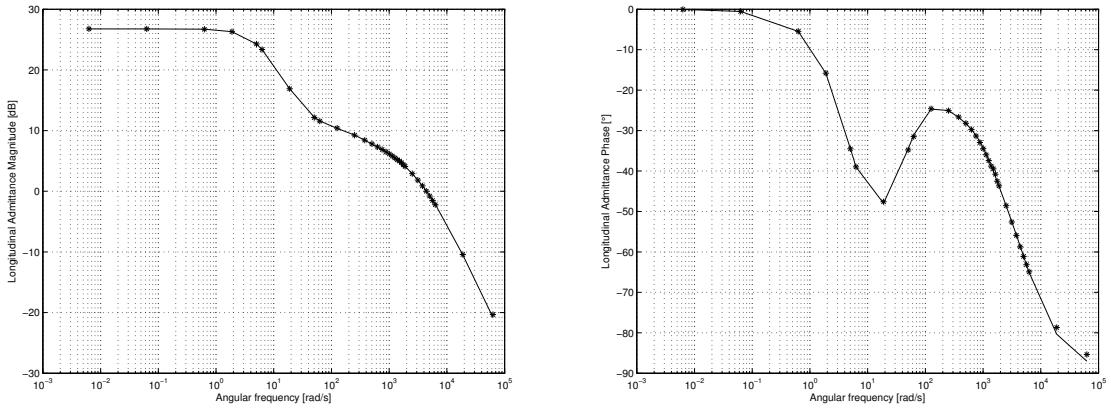

(a) (b)

Figure 4.2: Results of the optimum vector fitting for the longitudinal admittance of Cable 2 with the parallel of eigth RL series branches. The longitudinal admittance values found in PSCAD are highlighted in red, while the admittance of the parallel of the three series RL branches is depicted in blue.

The values of resistance and inductance of each branch are chosen in order to fit the frequency behaviour of the longitudinal admittance calculated in PSCAD. The developed script is available from authors. Figure 4.2 shows a good matching of the fitted values of the admittance by the eight parallel branches and the values calculated in PSCAD. The error on the admittance magnitude is never bigger than 1%, within 1000 Hz. The phase error is always less than 1.7°, in the frequency range of interest. Similar results are achieved for the cable with lower cross section, cable 1. The values used for later simulations are finally presented in Tables 4.1-4.2.

Table 4.1: Equivalent model parameters for cable 1.

Branch	1	2	3	4	5	6	7	8
$R\,[m\Omega]$	1053	1655	4000	1267	580	4212	3618	412
$L\,[mH]$	0.4	3.6	0.5	100.8	38.6	265.3	243.4	28.4

Table 4.2: Equivalent model parameters for cable 2.

Branch	1	2	3	4	5	6	7	8
$R\,[m\Omega]$	867	769	254	247	218	390	287	1433
$L\,[mH]$	3.0	0.5	47.0	45.5	40.3	56.0	52.5	0.3

4.2 Harmonic Susceptibility Study Setting

An harmonic susceptibility study is first performed with the accurate switching model implemented in PLECS.

The study case network with converters represented by their switching model is illustrated in Figure 4.3.

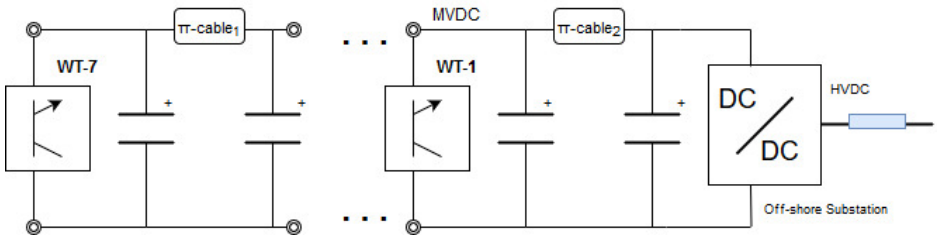

Figure 4.3: Wind farm network implemented with switching models of converters.

For the switching model, following simulation conditions are fixed for each wind turbine:

- The switching frequency coming from the feedforward path is fixed to 800 Hz;
- The input voltage is fixed to $4.04\,kV$;
- The output voltage is fixed by the network and the relative voltage drops, as it will be explained.

For the harmonic model, all the wind turbine converters are considered working around OP_2 (see Table 3.1), because the DC output voltage difference between wind turbines is not affecting the harmonic model parameters significantly.

A first consideration regarding the implementation of the network in PLECS is about the power flow between wind turbines. In order to obtain a power flow from the wind turbines to the network, the difference between the input voltage of the SRC# and the output voltage after the LC filter of the converter has to be sufficiently higher than 0 V. In first trial simulations, the problem of power flow appeared in the farthest wind turbine from the wind farm substation. The reason behind this problem was the voltage drop occurring in each line cable of the network.

Considering the flow direction of the current in the cables, each cable raises the voltage from the wind farm substation to the last wind turbine. In particular, with 100 kV at the substation terminals, the seventh wind turbine converter had an output voltage higher than the input voltage reflected on the grid side and so, the output current measured in the converter was zero ampere in steady-state. Therefore, in order to avoid this power flow problem, the voltage level at the terminals of the substation, modelled as a DC source, is fixed to 98.3 kV.

It is worth to notice the difference in the output current from each converter running with or without the controller. In particular, in the open loop configuration of the converters, all the output currents have different mean values. On the other hand, in the closed loop configuration, all the converter output currents are maintained constant by the action of each controller.

The disturbances coming from the offshore substation, produced by the DC/DC multilevel converter operation, are represented as an AC source. Sinusoidal voltage waves at different frequencies simulate disturbances. Amplitude is set at 500V, representing 0.5% of the nominal voltage magnitude in MVDC grid and with a frequency disturbance range between 20 and 300 Hz.

Simulations of disturbances in this model will be performed by frequency scan approach. The frequency of the superimposed disturbance is changed with a fixed time step. Saved data are analyzed by the means of the Fast Fourier Transform algorithm.

Finally, comparison at 100 Hz disturbance is avoided due to the mismatch observed in the harmonic model that would lead to high currents.

4.3 Comparison between Switching and Harmonic Model

One of the main advantages of the harmonic model developed is the time needed to simulate a large network with multiple wind turbines compared to a switching model. However, it is a choice between accuracy and simulation time. In the harmonic model, higher order harmonics are not taken into account, and the interaction between wind turbine converters is not always well described for a cluster of several wind turbines.

Results of the switching model and the harmonic model are compared for the operating conditions introduced in section 4.2. First the general trend of magnitude and phase of the output current for both model is analyzed. The open and closed loop results are illustrated in Figure 4.4 and in Figure 4.5 respectively. As immediate comment, it can be seen that the mismatch between switching and harmonic model starts to be significant from the fifth wind turbine until the farthest wind turbine, WT 7.

The maximum amplitude of the fundamental harmonic current is reached in the closed proximity of the resonant frequency of the filter, while it is lower near the edges of the test frequency range. It is significant to mention that, at critical frequencies around the resonant frequency of the filter, a disturbance of 0.5% on the output voltage leads to around 8.5% disturbance on the current. Consider for example the fourth wind turbine, operating in open loop (see Figure 4.4, WT4). The voltage disturbance of 500V at $120Hz$, is responsible for a fundamental harmonic current around $5.5A$ for both models. At $20Hz$ the harmonic current amplitude drops around $1A$, while at $300Hz$ it is $1.2A$. This trend is respect by all the wind turbines except for the last one, as described later in detail. For closed loop simulations, the trend of fundamental harmonic current amplitude is similar.

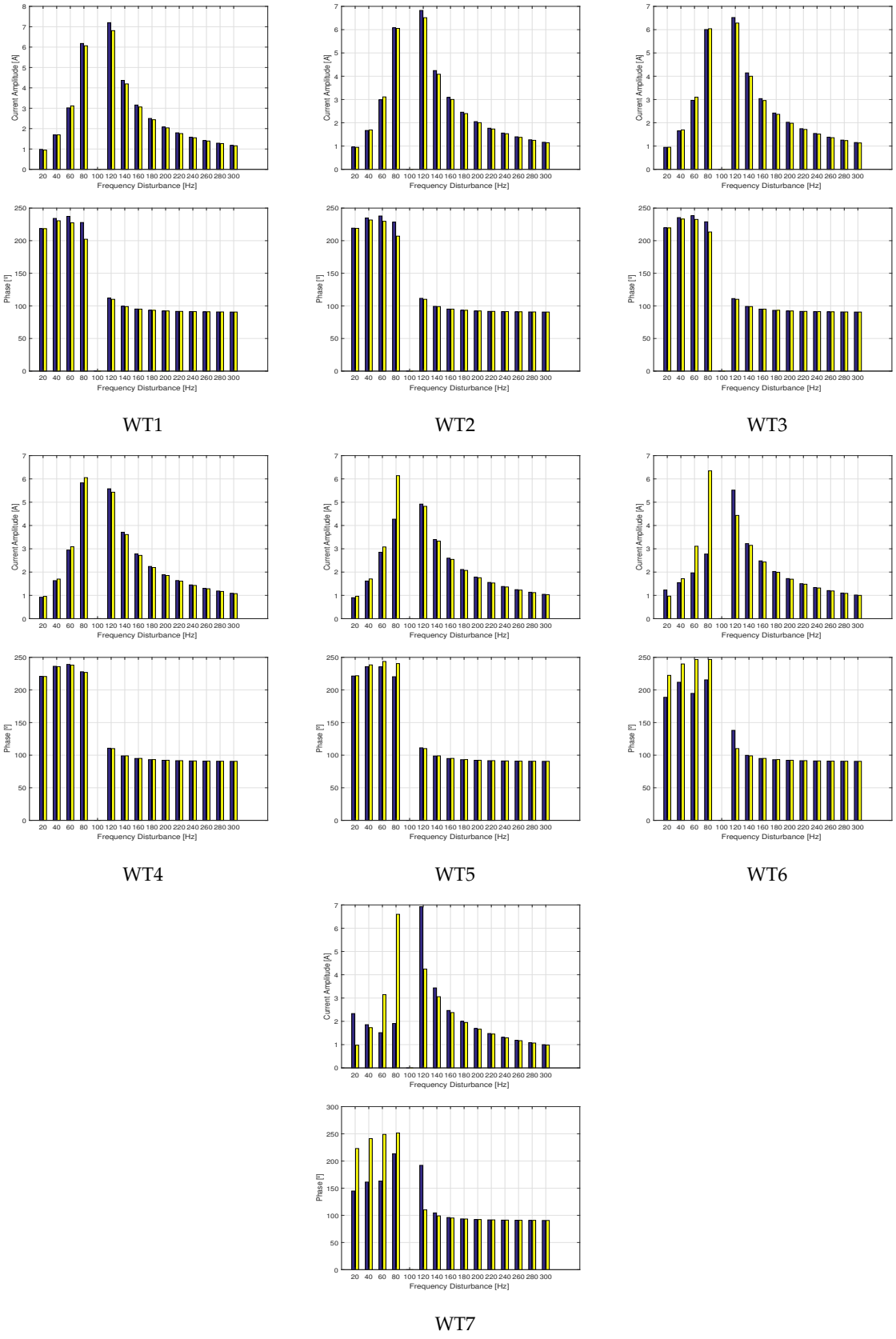

Figure 4.4: Open Loop network model. Spectrum of output currents for each wind turbine of the network. For each wind turbine: harmonic current amplitude [A], harmonic current phase [°]. Switching model (Blue line) and harmonic model (Yellow line).

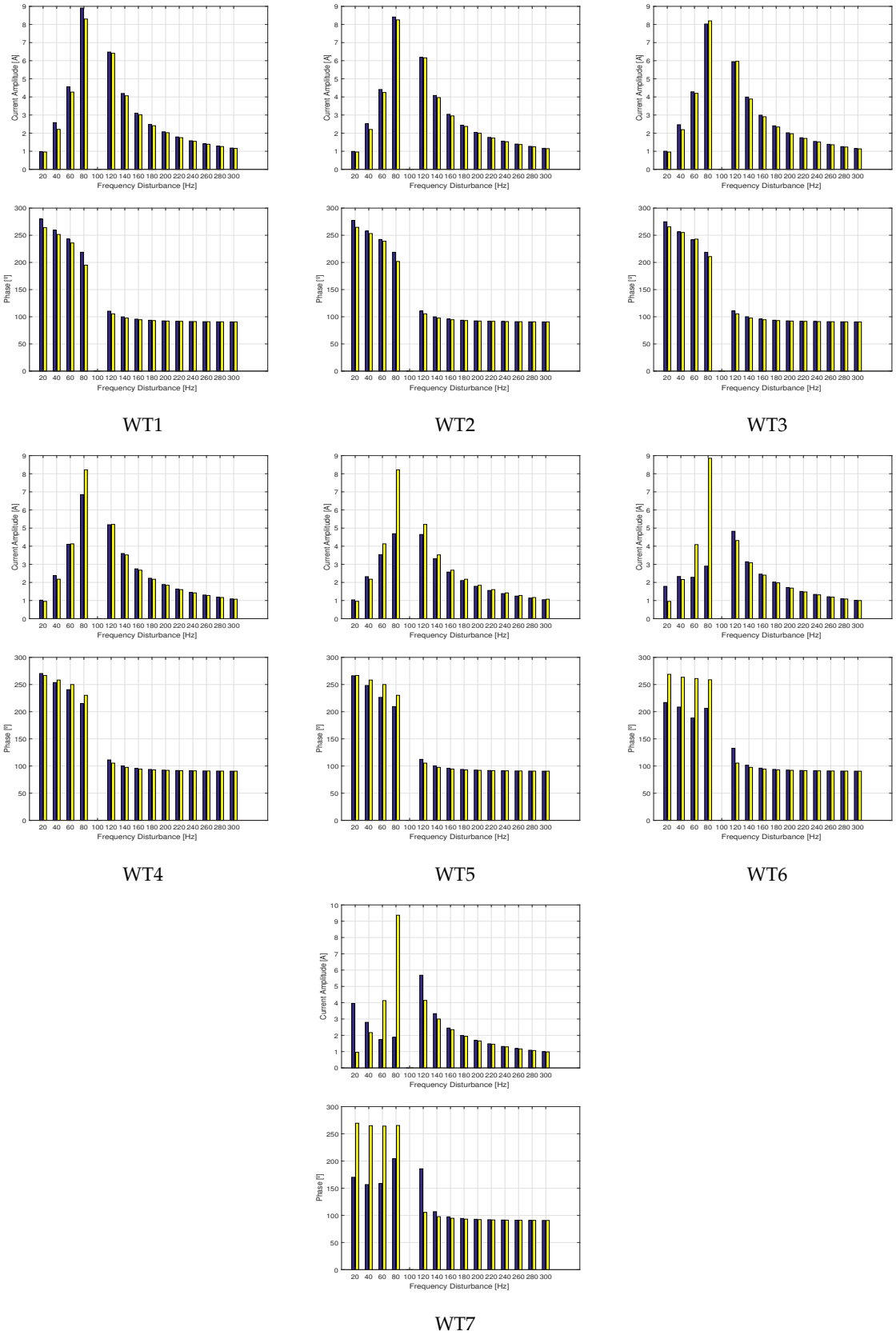

Figure 4.5: Closed Loop network model. Spectrum of output currents for each wind turbine of the network. For each wind turbine: harmonic current amplitude [A], harmonic current phase [°]. Switching model (Blue line) and Harmonic Model (Yellow line).

Difference between both models in the first wind turbines can be understood from the mismatch in the admittance equivalent introduced in section 3.7. However, big differences appear at low frequencies in the last wind turbines. This is explained due to the non linear switching behaviour of converters, that creates harmonics at multiples of the fundamental frequency. The equivalent model foresees similar amplitudes for the current harmonics flowing in each wind turbine. However, according to the switching model, the amplitude of the fundamental current harmonic decrease along the cluster, approaching the farthest wind turbine from the substation. This phenomenon is related to the rising amplitude of higher order harmonics as depicted in Figure 4.6 and Figure 4.7.

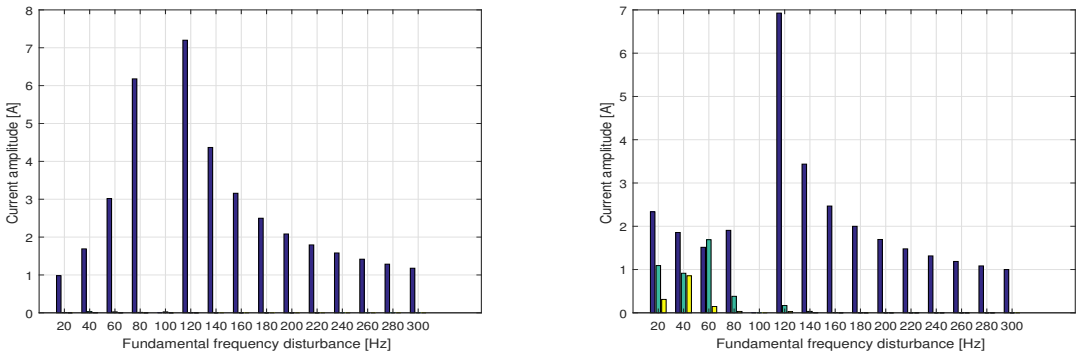

(a) (b)

Figure 4.6: Current harmonics in the open loop switching model. First order harmonic (Blue line), second order harmonic (Green line) and third harmonic (Yellow line).

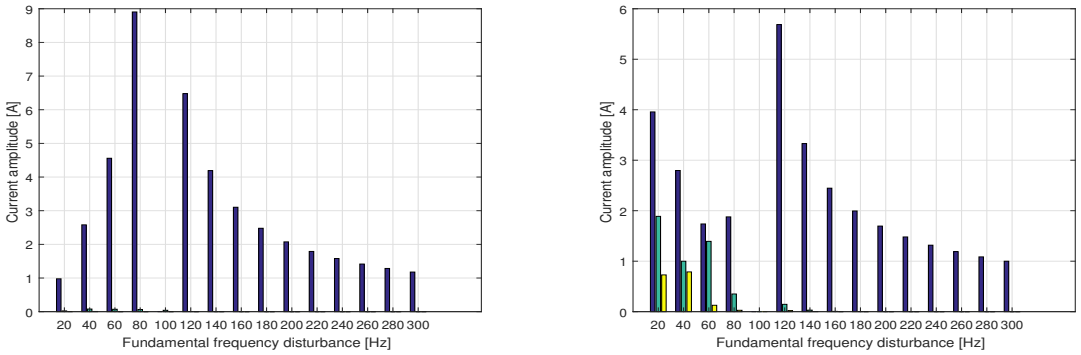

(a) (b)

Figure 4.7: Current harmonics in the closed loop switching model. First order harmonic (Blue line), second order harmonic (Green line) and third harmonic (Yellow line).

The effect of the higher order harmonics is relevant only in the last wind turbines (see Figure 4.8), as also the voltage disturbance across these wind turbines ends up being different from a sine wave.

In order to explain this phenomenon consider as starting point the closest wind turbine to the offshore substation. It is draining a really small second order harmonic current from the grid, causing a small voltage drop across the longitudinal admittance connecting the wind turbine to the substation. The next wind turbine requires as well a second order current harmonic, higher than before, because a second order harmonic voltage is already appearing across the previous wind turbine. The phenomenon is amplifying as the farthest wind turbines are approached.

Same reasoning is valid for current harmonics higher than the second. Higher order harmonics do not always sum each other directly along the cluster, due to phase shifts. Thus, it is not possible to predict the amplitude of the higher order harmonics in the cables from the amplitude of higher order harmonics flowing in the wind turbines.

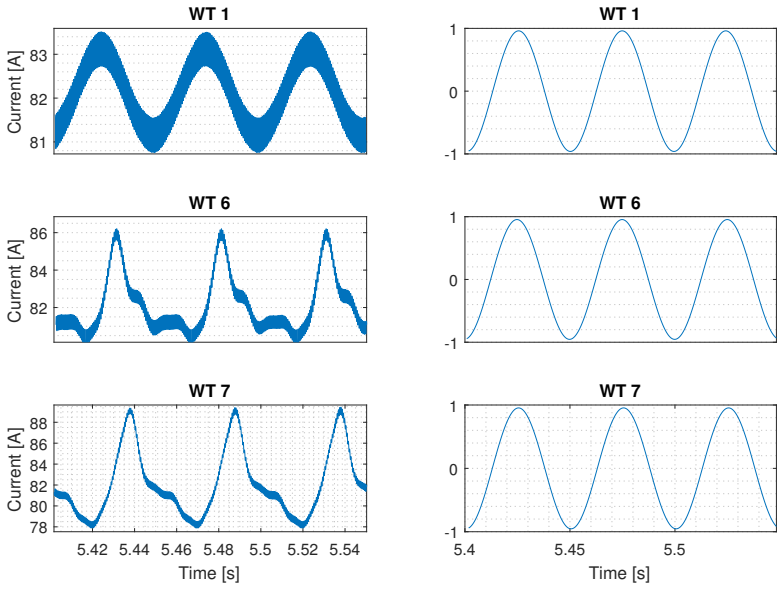

Figure 4.8: Comparison in closed loop network of the converter output currents (i_n) between switching (left graphs) and harmonic (rigth graphs) models for a disturbance at 20 Hz.

From PLECS simulations, harmonic currents at 1600 Hz, double the switching frequency, are observed. These harmonics appear also without the presence of any voltage disturbance from the MVDC substation, see Figure 4.9. This is consistent with the fact that the filter is only attenuating the fundamental due to the operation of the converter itself.

As it can be seen in Figure 4.9, these high frequency current harmonic add together in each cable, reaching an amplitude of $3.15A$ in the offshore substation. This current harmonic could originate issues in the multi-level converter.

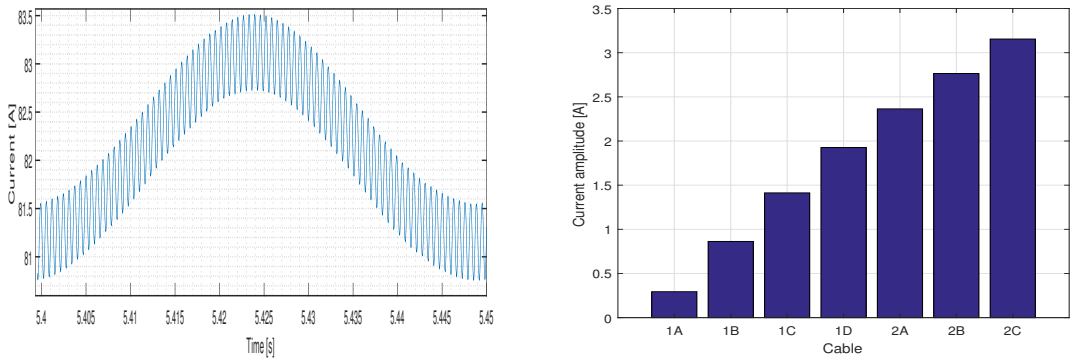

(a) (b)

Figure 4.9: (a)Example of harmonic currents at 1600 Hz on top of a 20 Hz disturbance. (b) Current amplitude at 1600Hz harmonic frequency in each cable of the wind turbine cluster.

Chapter 5

Experimental Results

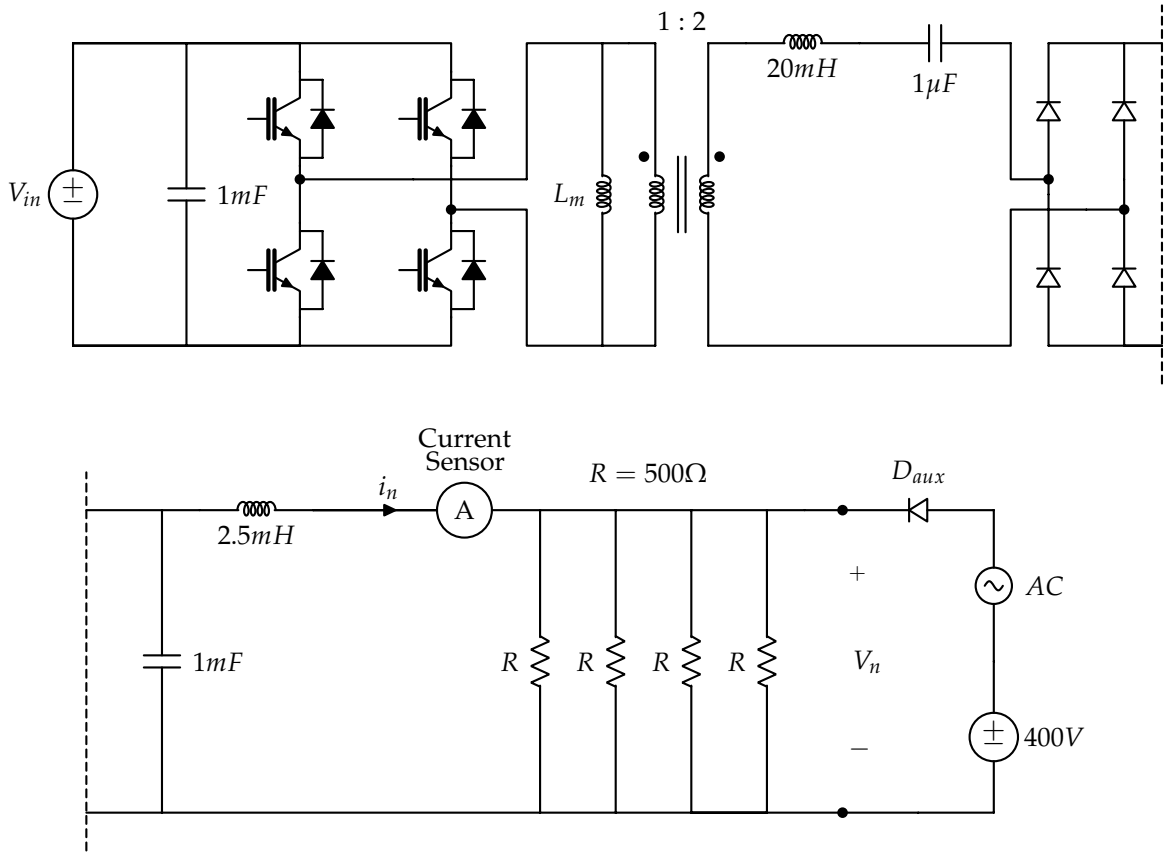

Figure 5.1: Scaled-down system schematic

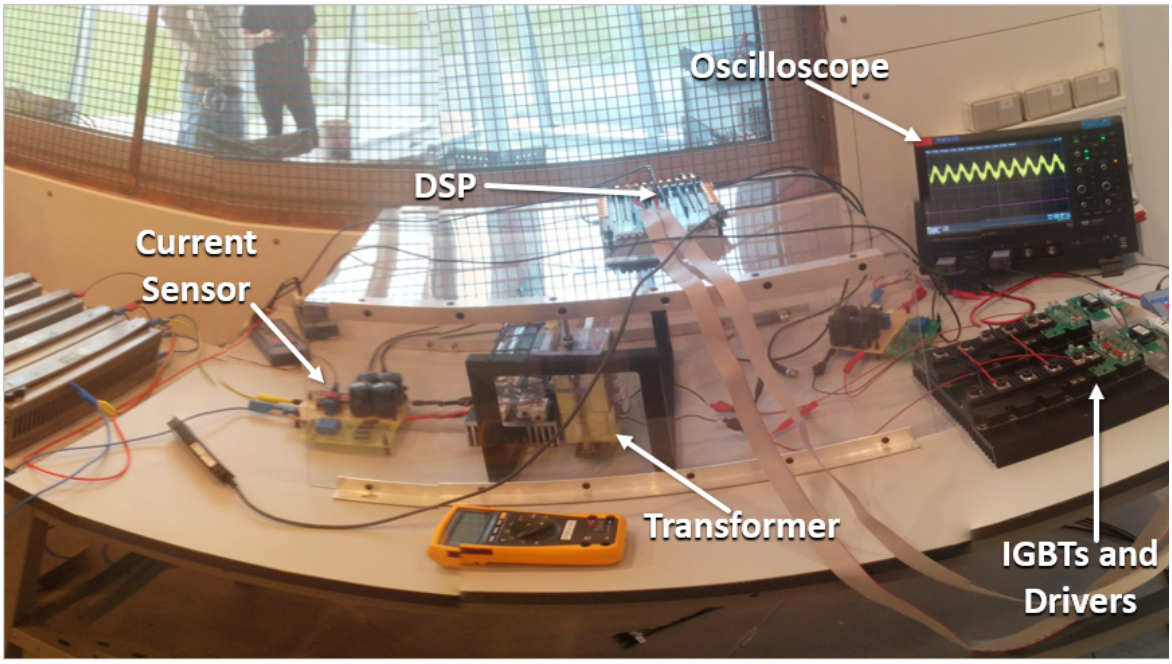

Figure 5.2: Scaled-down setup of SRC#

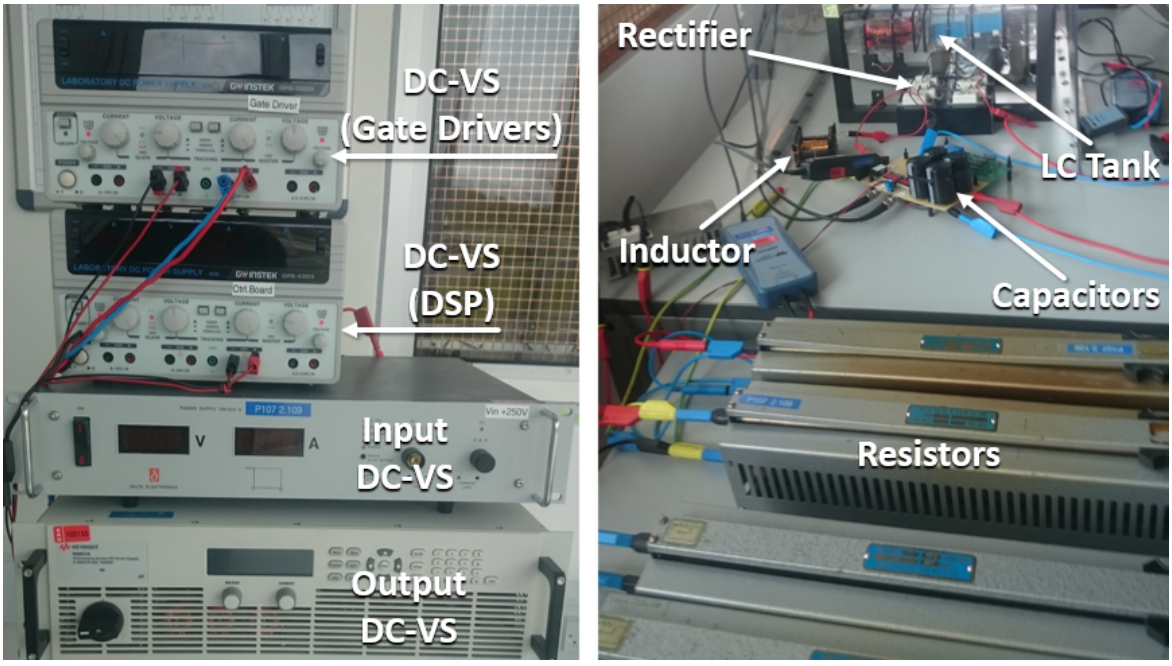

Figure 5.3: DC sources and components of the scaled-down system

Once some analyses based on control design and harmonic susceptibility were done, an experimental scaled-down setup of the SRC# was tested in the laboratory for one op-

erating point. In this case, the provided power, output voltage and switching frequency were 549.7 W, 400 V and 800 Hz respectively. The schematic of the system is described in Figure 5.1, and the equipment and components to setup the system are depicted in Figure 5.2 and Figure 5.3. In this scaled-down system an auxiliary diode is placed due to the fact that the available voltage sources on the output side are not able to consume power. On the other hand, the input voltage in the scaled-down system has been increased 11 V respect to the input voltage used in simulation (205 V), in order to reach 216 V. This is because losses and voltage drops are not considered in simulation, and the voltage on the turbine side of the transformer has to be the same in order to have similar operating points. Additional information about components and equipment for the scaled-down system is given in Appendix B.

5.1 Control Algorithm

A digital signal processor (DSP), model TMS302F28379D was used to code the control algorithm, which was responsible for generating four PWM signals (EPWM1A, EPWM1B, EPWM2A, EPWM2B) and one A/D conversion. The former uses four submodules of the pulse width modulation module of the DSP. The first submodule called Time-base (TB) is used to set the switching frequency, the second named Counter-compare (CC) to set the duty cycle. The next one is the Dead-band (DB) submodule to establish a delay between complemented pulses, and the last one, called the Action-qualifier (AQ) submodule, settles the instant when the high and low levels of the PWM signals occur, and a delay equal to half of the resonant period ($T_r/2$) between the legs of the converter, in order to accomplish the pulse removal control technique. On the other hand, the Analog-to-Digital module of the DSP was used for output current sensing. The channel $A0$ was configured to work with a 12-bit resolution and sample-and-hold acquisition time equals 150 ns. Also, an interruption after each A/D conversion was configured, and an internal ePWM is used to trigger the ADC, whose sampling frequency is 50 kHz.

The control algorithm has been implemented by considering the following criteria. First, initialization functions are used to set up the code. Then, every single needed variable is created, and the peripherals are configured. Once the ADC is completed, the ac-input value is saved as binary number in an internal vector. After that, the average current is calculated when the EPWM1A signal output toggles. As a result, the digital controller sampling frequency (f_s) is always twice the switching frequency (f_{sw}) of the SRC#. Next, the small switching frequency change (f_{sw_ss}) is obtained mathematically by using a difference equation of the controller, which considers the actual and previous values of the average current and switching frequency. Finally, the control algorithm includes as feedforward the frequency of the operating point ($f_{sw\_op} = 800\,Hz$), so the switching frequency is updated only by a small change. The flow chart in Figure 5.4 shows how the control algorithm works.

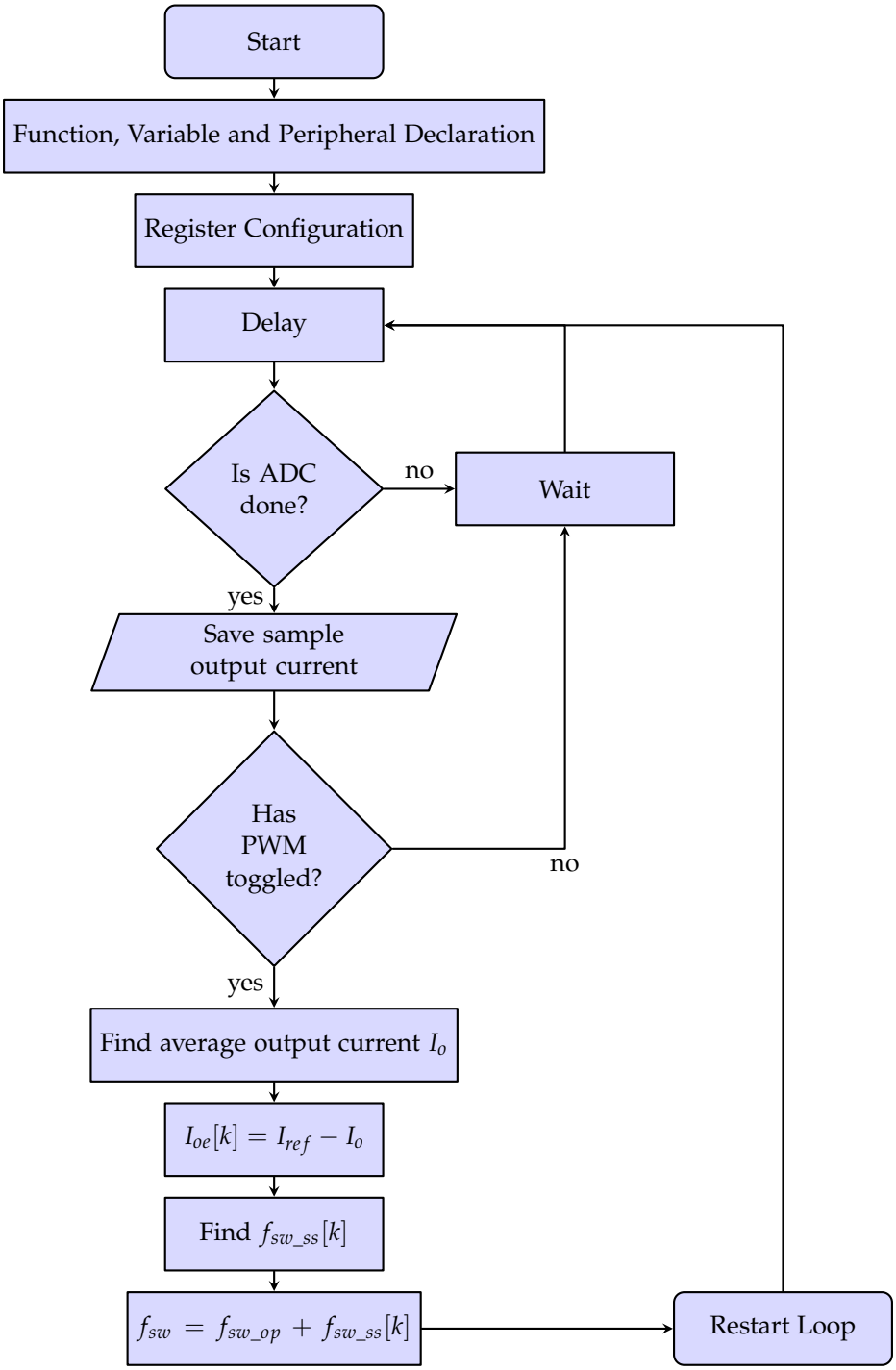

Figure 5.4: Flow chart of the control algorithm

5.2 SRC # Operation Mode

The operation mode of the scaled down setup is also depicted in Figure 5.5, where the reverse recovery phenomenon of the diodes and discontinuous conduction mode are seen. The former has been neglected in simulation. Also, from the voltage waveform is seen that the pulse removal control technique has been implemented satisfactorily. Either stray resistance, filter effect and diode reverse recovery current have an impact on the voltage and current waveforms of the converter.

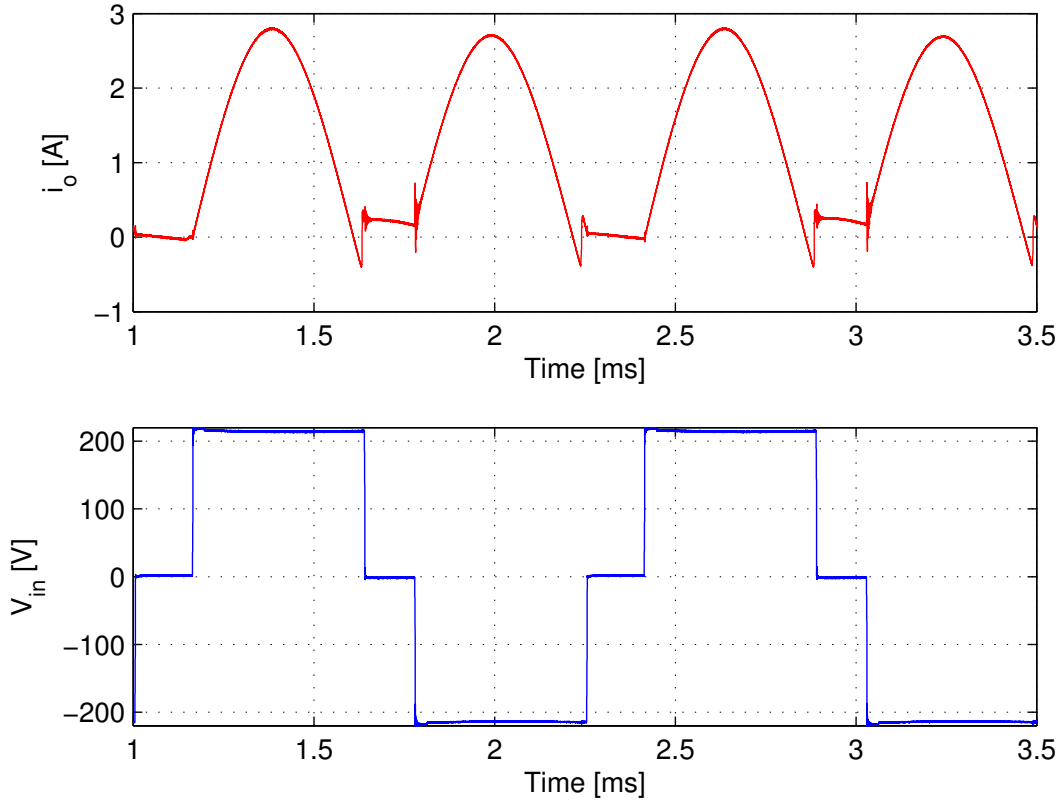

Figure 5.5: Output current (red) and voltage on the turbine side of the transformer for the scaled down converter in the operating point defined in Table 5.1

Table 5.1: Operating Point for the harmonic tests on the Scaled Down Setup.

V_{in}	V_{out}	f_{sw}	i_n	P_o
$216V$	$400V$	$800Hz$	$1.37A$	$547.9W$

5.3 Dynamic Response Analysis

To analyze the controller and system behavior, first some simulations have been carried out with PLECS, and then the scaled-down system has been tested. Figure 5.6 (a) shows the dynamic response of the system when a negative step input signal of 4 V was applied on the output voltage, and the system works in open loop (Output power supply: Chroma 61511). It can be seen that the responses between simulation and test result do not fit because some stray resistances are not considered in simulation. This mismatch is also due to the finite dynamic performances of the output voltage source, that requires a finite time to decrease the voltage. It is clear that decreasing the output voltage brings about a higher output current.

Likewise, three test in closed loop were done with three different step input signals (Output power supply: Keysight N8957A). Figures 5.6 (b) and (c) depict the system re-

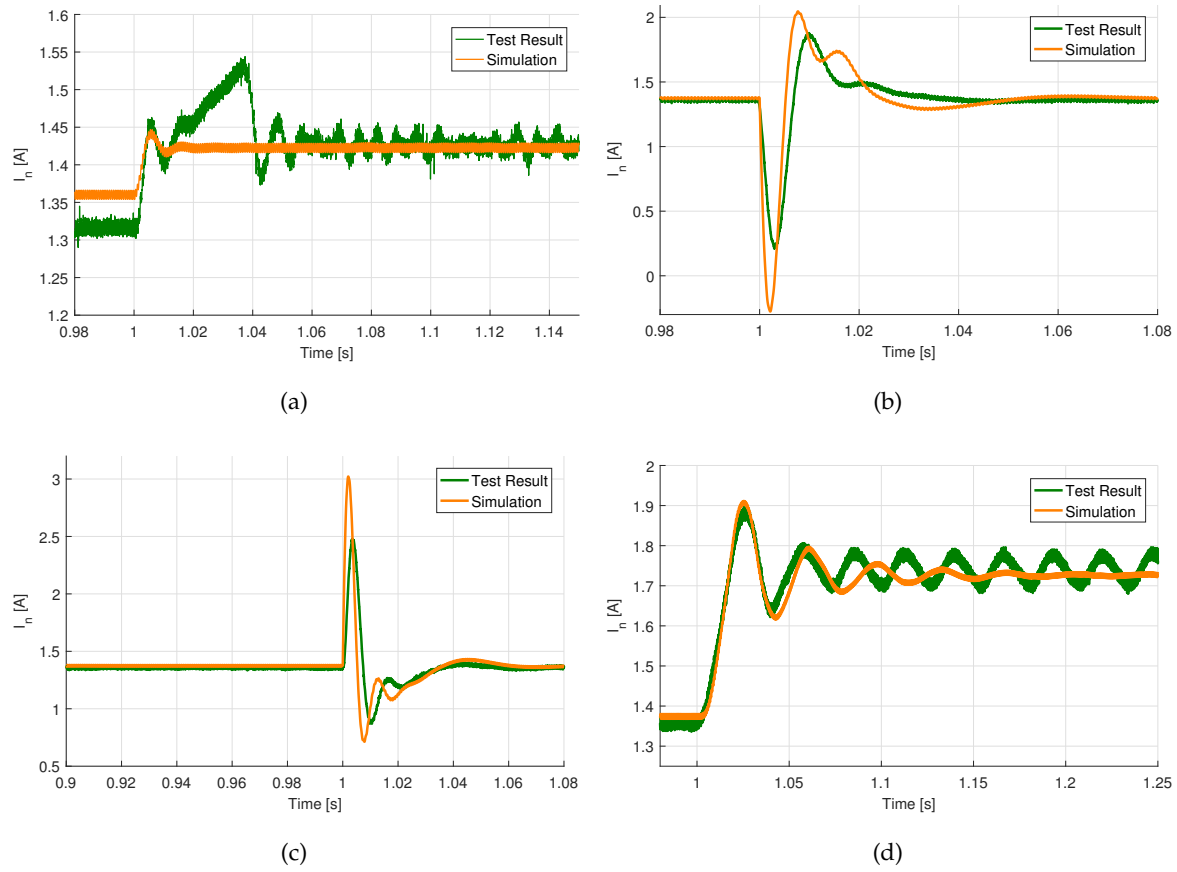

Figure 5.6: Dynamic response of the current when (a) 4 V step-down signal is applied in the output voltage in open loop, (b) 4 V step-up signal in the output voltage in close loop, (c) 4 V step-down signal in the output voltage in close loop, and (d) (1.37A $\rightarrow$ 1.73A) step-up signal in the reference power in close loop.

sponse when a positive and a negative step in the output voltage are applied respectively. The system exhibits similar behavior either simulation or experimental test. Again, stray resistance has an impact in the response amplitude; however, the controller is able to track the reference current. Similarly, the Figure 5.6 (d) represents how the output current behaves when a step signal is applied in the reference current ($1.37A \rightarrow 1.73A$). In both cases, simulation and test result, the controller is able to keep the output current close to its reference. The oscillations in the experimental test of Figure 5.6 (d) are due to the diode D_{aux} (Figure 5.1) which is reverse biased at some instants. All the above results give enough supporting arguments to test the converter with specific harmonic disturbances.

5.4 Harmonic Susceptibility Study

The major objective of the mathematical small signal model developed for the SRC# Converter is the study of the current harmonics in the DC power collection grid, thus some tests of the current harmonics in response to voltage disturbances have been performed, around the operating point described in Table 5.1.

A programmable AC source has been used to apply the DC voltage of 400 V and superimpose a disturbance of $3.5V_{RMS}$ at different frequencies in the range $20Hz - 300Hz$. The foreseen low DC current for the load resistor, brought to the reverse biasing of the auxiliary diode for some test frequencies, as illustrated from Figure 5.7 to Figure 5.10. When the voltage on the filter capacitor is high enough, and the load current is too low, the diode can stop its conduction, and this results in the capacitor discharging on the load resistor. During these time intervals, the voltage imposed from the AC source is applied to the auxiliary diode instead of the scaled down converter.

By inspection of Figures 5.7 to 5.10 is evident that is not possible to compare the test results obtained for test frequencies around the resonant frequencies with the harmonic model, due to the lack of application of the voltage on the output side for some time intervals. As recommendation for future experiments, a bidirectional power flow source should be used in order to feed the output side of the converter, or a bigger load should be chosen. For test frequencies until 60 Hz and higher than 200 Hz, the diode conduction is always guaranteed and the harmonic model results show good accordance with both test results and PLECS simulations, as portayed in the following Figure 5.11 and Figure 5.12.

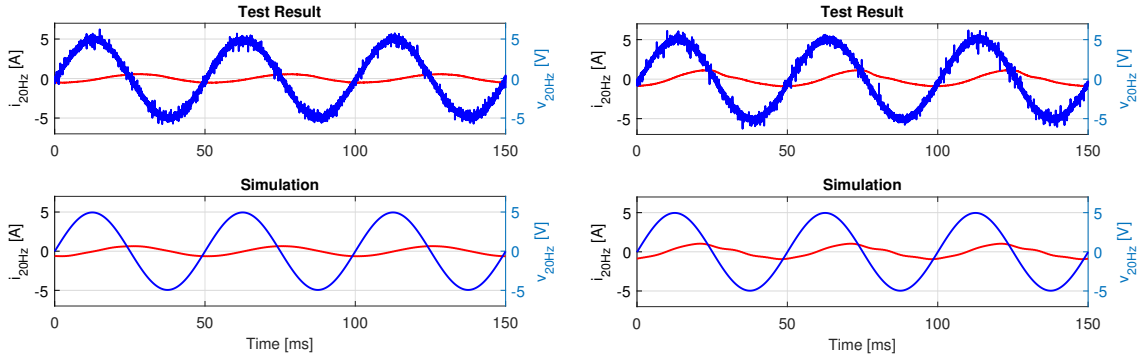

(a) 20 Hz Open Loop

(b) 20 Hz Closed Loop

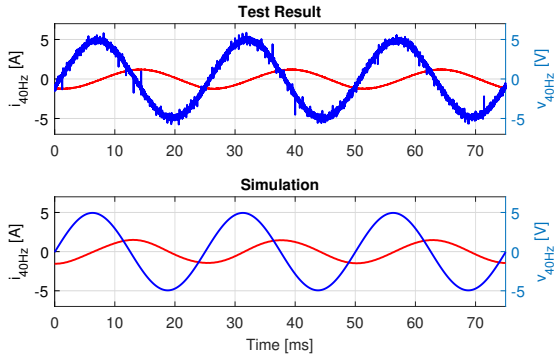

(c) 40 Hz Open Loop

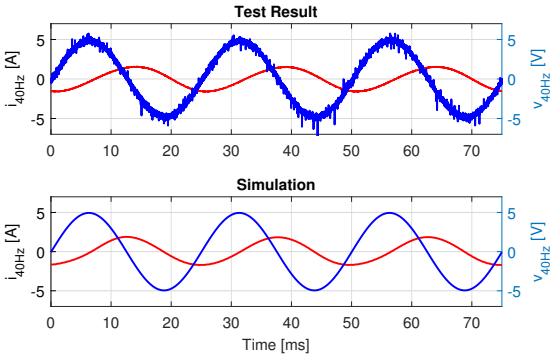

(d) 40 Hz Closed Loop

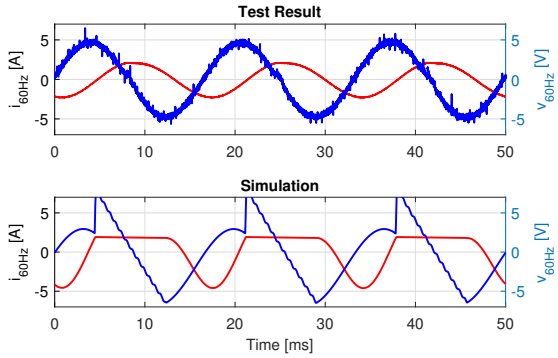

(e) 60 Hz Open Loop

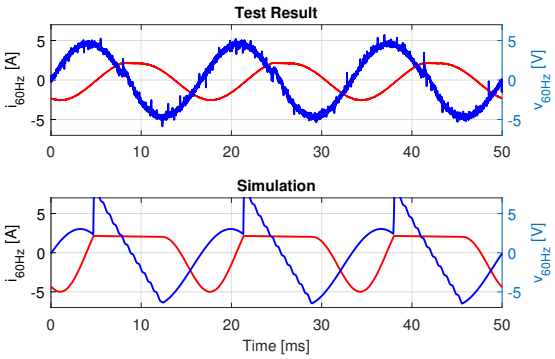

(f) 60 Hz Closed Loop

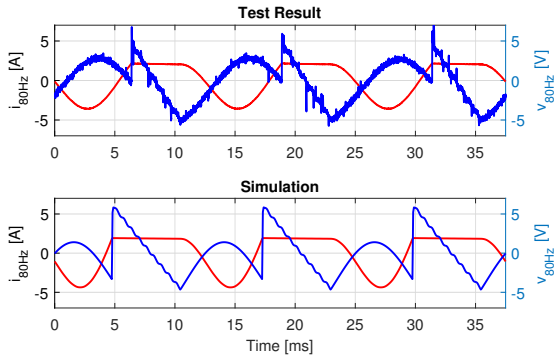

(g) 80 Hz Open Loop

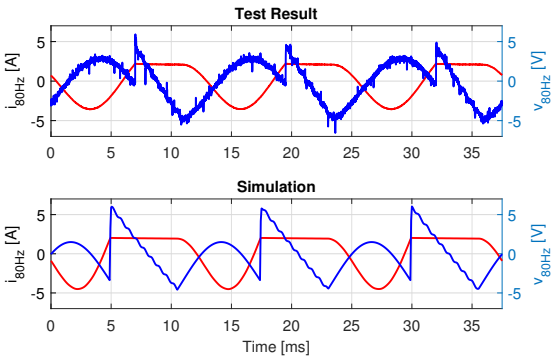

(h) 80 Hz Closed Loop

Figure 5.7: Current (red) and voltage (blue) output waveforms when a perturbation from 20 to 80 Hz is injected .

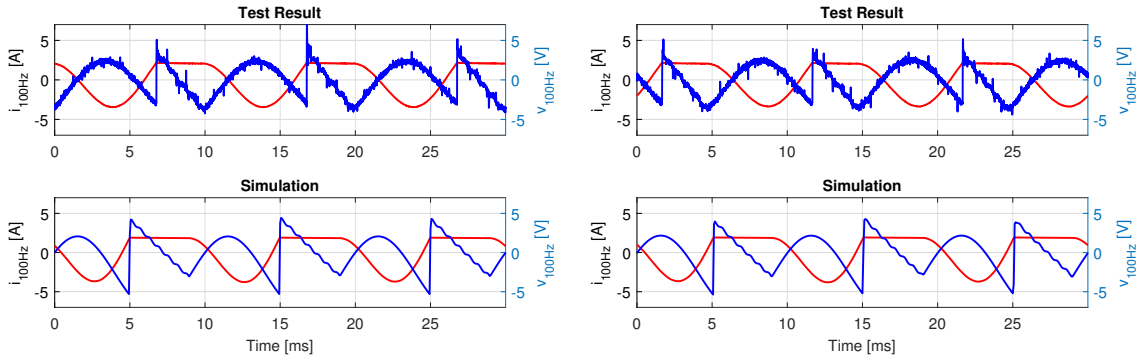

(a) 100 Hz Open Loop

(b) 100 Hz Closed Loop

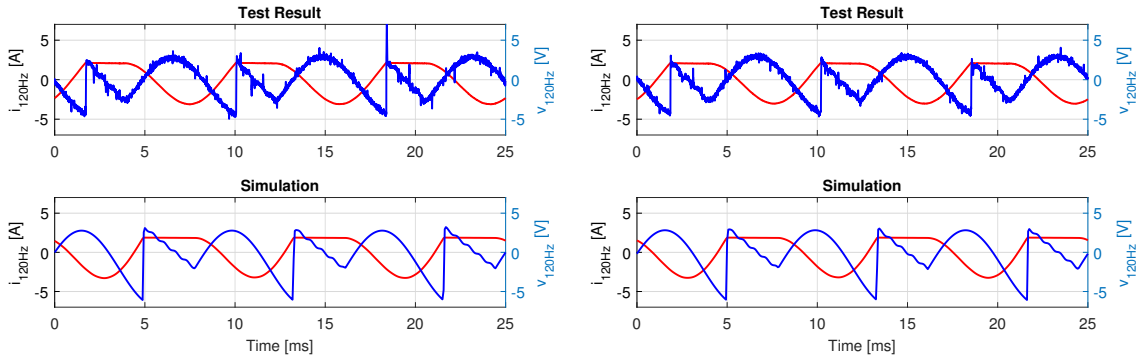

(c) 120 Hz Open Loop

(d) 120 Hz Closed Loop

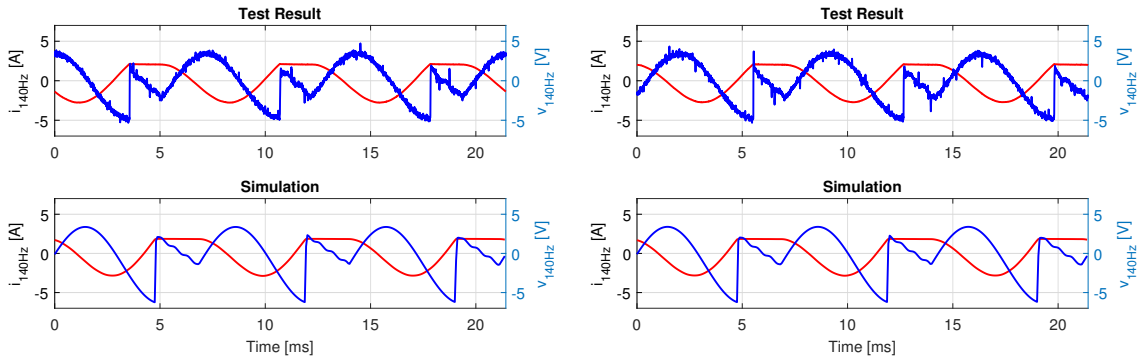

(e) 140 Hz Open Loop

(f) 140 Hz Closed Loop

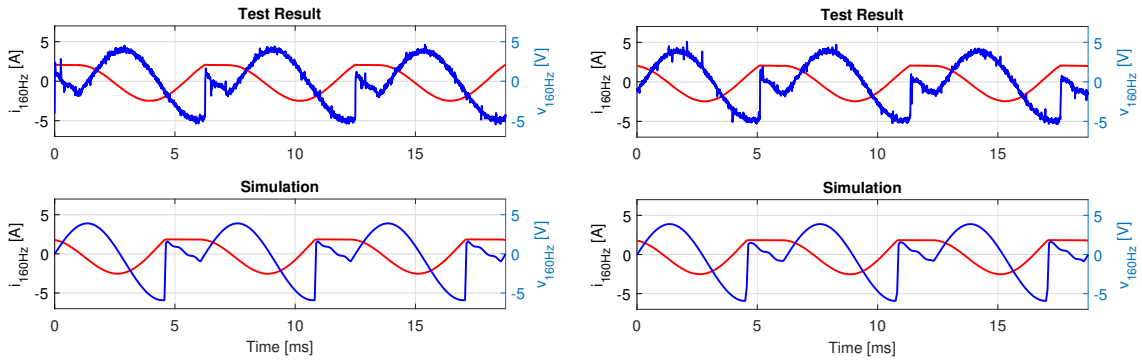

(g) 160 Hz Open Loop

(h) 160 Hz Closed Loop

Figure 5.8: Output current (red) and voltage (blue) waveforms when a perturbation from 100 to 160 Hz is injected .

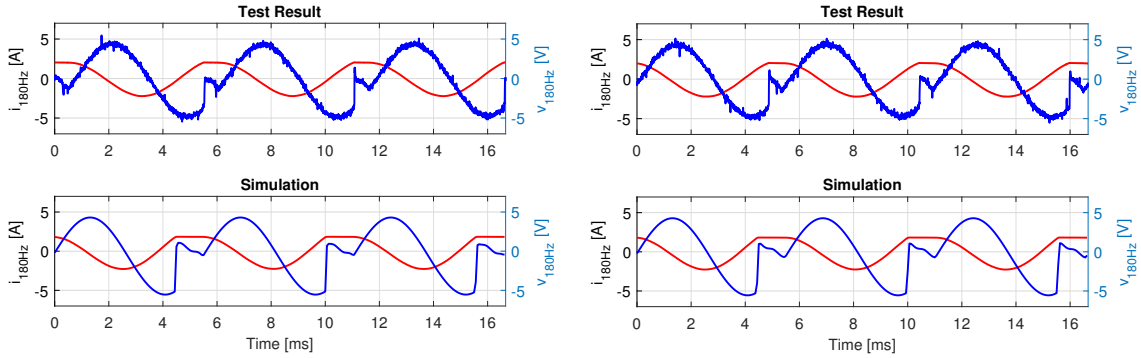

(a) 180 Hz Open Loop

(b) 180 Hz Closed Loop

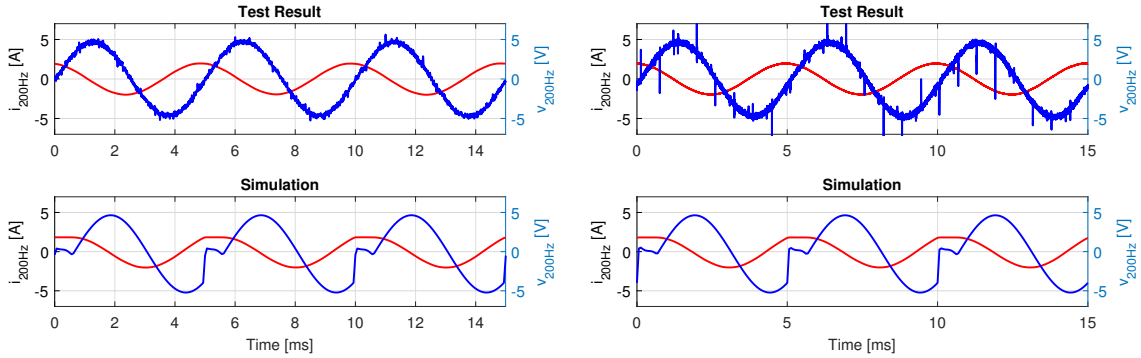

(c) 200 Hz Open Loop

(d) 200 Hz Closed Loop

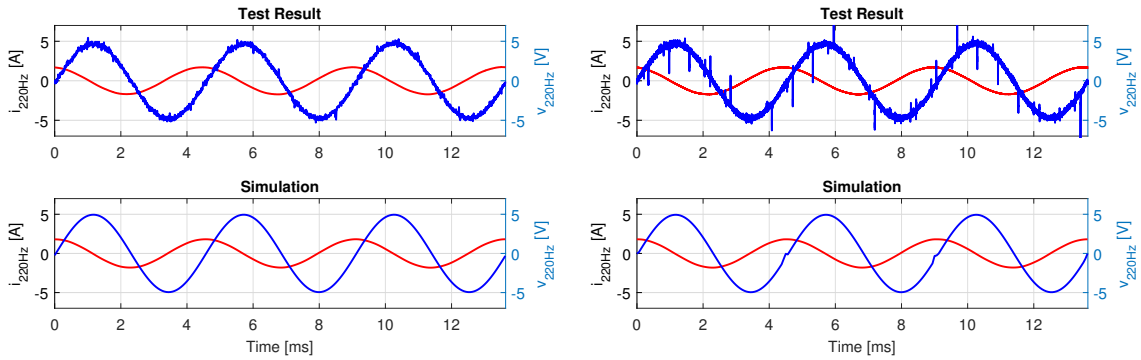

(e) 220 Hz Open Loop

(f) 220 Hz Closed Loop

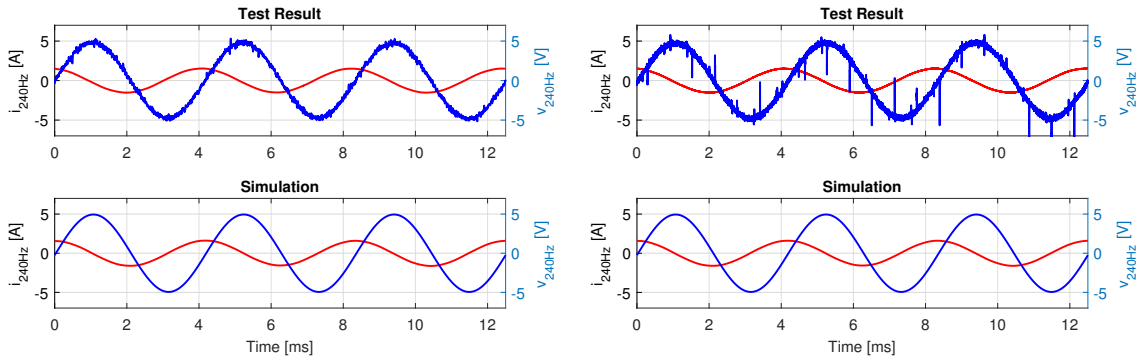

(g) 240 Hz Open Loop

(h) 240 Hz Closed Loop

Figure 5.9: Output current (red) and voltage (blue) waveforms when a perturbation from 180 to 240 Hz is injected .

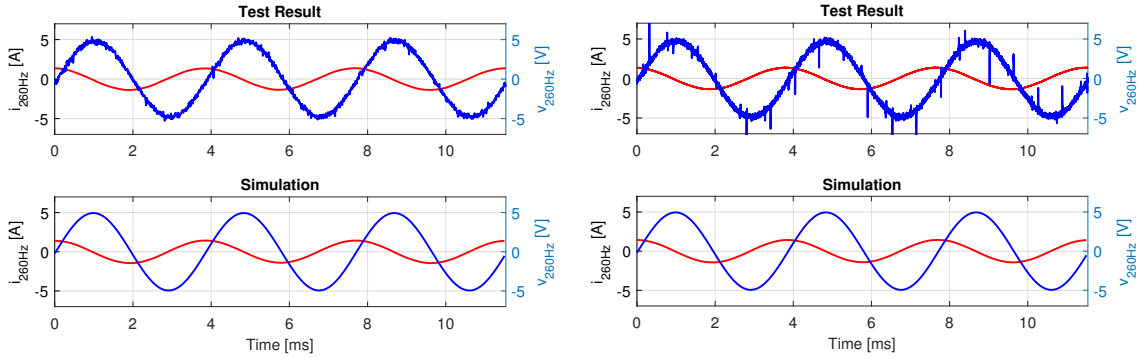

(a) 260 Hz Open Loop (b) 260 Hz Closed Loop

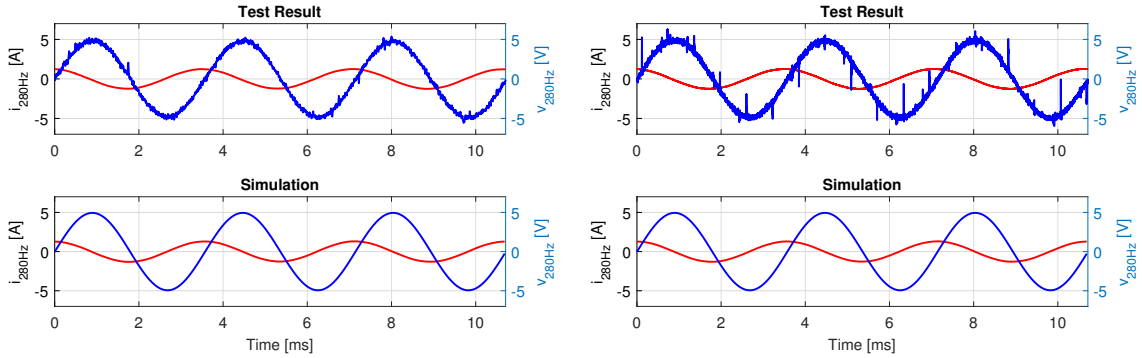

(c) 280 Hz Open Loop (d) 280 Hz Closed Loop

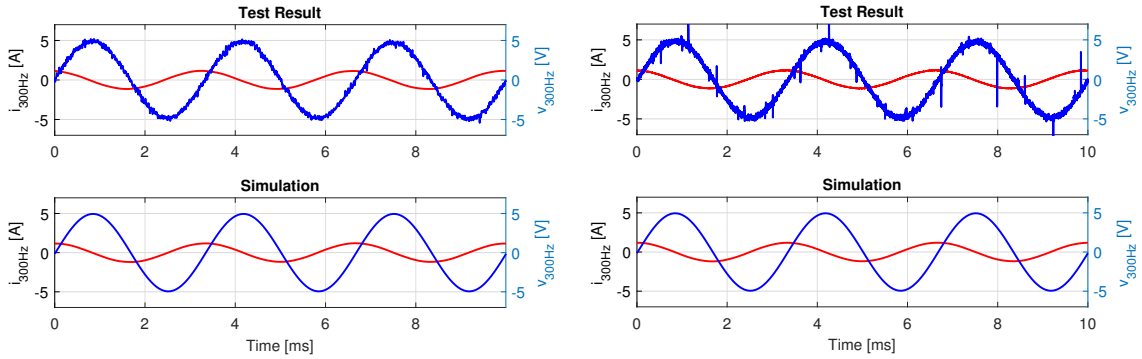

(g) 300 Hz Open Loop (h) 300 Hz Closed Loop

Figure 5.10: Output current (red) and voltage (blue) waveforms when a perturbation from 260 to 300 Hz is injected .

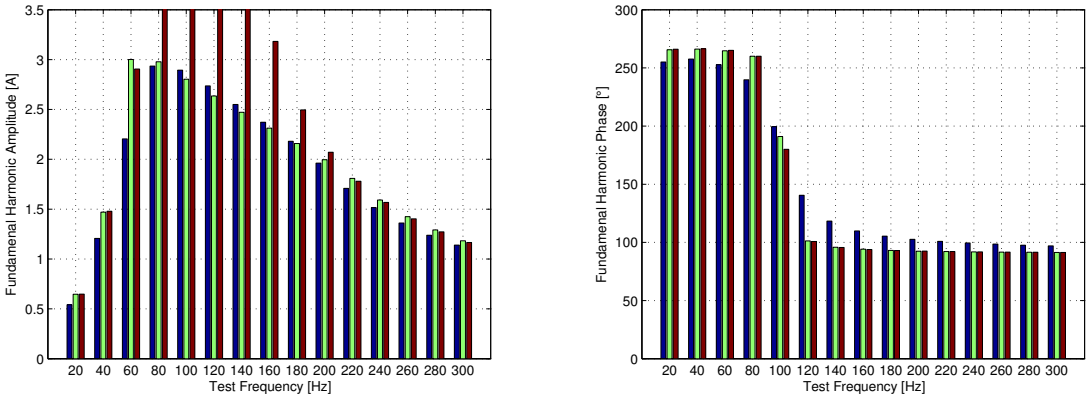

(a) (b)

Figure 5.11: Fundamental harmonic current for disturbances of $3.5V_{RMS}$ on the grid side at different test frequencies, without controller: (Blue line) Laboratory test; (Green line) PLECS simulation; (Red line) Harmonic model

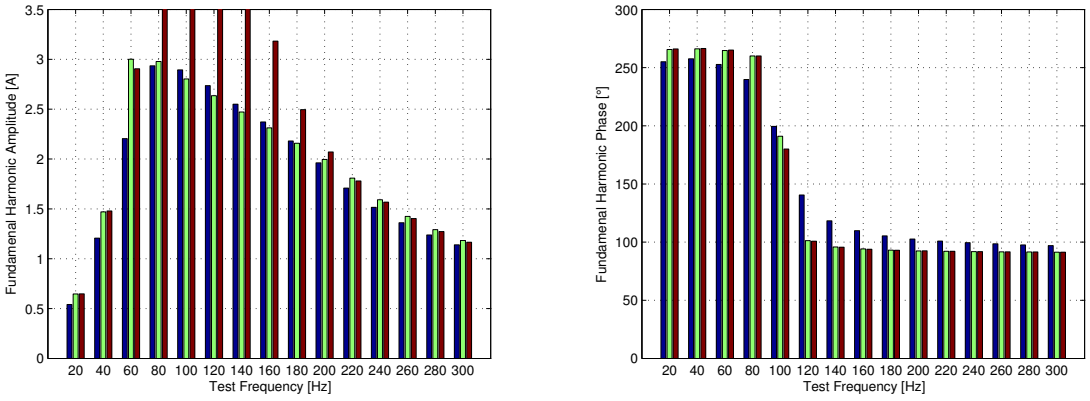

(a) (b)

Figure 5.12: Fundamental harmonic current for disturbances of $3.5V_{RMS}$ on the grid side at different test frequencies, with controller: (Blu line) Laboratory test; (Green line) PLECS simulation; (Red line) Harmonic model

Chapter 6

Conclusions

In section 6.1 main difficulties found in the project, dealing with the control of the SRC #, will be shown. Section 6.2 is a final evaluation of the proposed harmonic model for susceptibility study of the DC power collection grid. Finally section 6.3 suggest the paths to undertake for a better understanding of the SRC # and the Harmonic susceptibility study of the DC power collection grid.

6.1 Control Challenges

The main difficulty in the development of the project has been represented by the implementation of the controller in the PLECS switching model. The problems are mainly related to the discretization of the transfer function of the controller, previously built in the continuous time domain. The reader should consider in particular:

- The discretization time step is not arbitrary but established by the behaviour of the converter itself. The switching frequency can only be varied once a discrete event is completed, so the discretization time step turns out to be around half of the switching period.
- The discretization time step is not fixed: the controller itself, varying the operating switching frequency in response to disturbances, is modifying the time interval between two discrete events.
- The dynamic performances of the control system are heavily limited by the small discretization time for the considered switching frequency range. It results that around 30 samples are required in the settling time to have good accordance between the small signal model and PLECS simulations.
- The small discretization time step does not allow to delete the complex imaginary poles of the filter. The foreseen frequency variation in response to a step in the

reference current leads to a fast overshoot in the continuous time model, that lasts less than the discretization time step.

In order to overcome these drawbacks, some endeavors have been done. First, the controller has been built directly in the discrete time domain. Only few improvements in the performance were obtained following this path. Moreover, the modeling of the converter in the continuous time domain would have been more complex.

In a following stage an attempt has been done to design a SRC# operating in the switching frequency range $[6000 - 10000]Hz$. As a result, higher performance of the controller have been achieved, allowing for the control system settling times up to ten times smaller than the ones obtained in the developed study case. Also the resonant frequency of the filter can be higher in this case, with economic savings on the filter. There are two main drawbacks to take into account. The switching losses will be certainly higher, and the converter should be sized for lower power ratings, or several SRC# converters should be used in parallel for the connection of one wind turbine to the DC grid. This would give some redundancy and would improve reliability, but higher costs for insulation would be a major problem.

On the other hand, even if an higher switching frequency is achieved, this does not necessarily result in the increase of the resonant frequency of the LC filter. Considering the developed harmonic susceptibility study, the resonant frequency of the filter should be set to a lower value than the typical switching frequency of the offshore substation converter, in order to avoid the amplification of current harmonics in the DC power collection grid.

6.2 Results from the Simulations

Harmonic disturbances in the medium voltage of the offshore substation lead to important current harmonics in the output of the DC/DC wind turbine converters. Due to the high complexity of the converter and controller of each wind turbine in a large network, an admittance equivalent for harmonic study is a simplified, time-saving and well-approached method to study the impact of such disturbances. However, this equivalent model does not describe the behaviour of the converter for other frequencies than the fundamental and in the case of a large network, it is important to consider a switching model in order to be closer to reality.

Characteristics of the designed controller result in a rejection of the disturbances in a narrow low frequency range. Around the resonant frequency of the output filter of the converters, the impact of grid voltage perturbations on output harmonic currents is critical. Moreover, relevant 2^{nd} and 3^{rd} current harmonics appear in the farthest wind turbines from the offshore substation, due to the non-linearity of the components in the converter. Additionally, current harmonics at twice the switching frequency are present at converters' output. These high frequency currents add up together in the grid, and their sum turns out to be relevant in the closed proximity of the offshore substation.

From the results of chapter 4, the developed harmonic model represents a good solution to perform an harmonic susceptibility study of the DC power collection grid only for disturbances at frequencies sufficiently higher than the resonant frequency of the output filter of each SRC # converter. At these frequencies the amplitude of current harmonics is also small compared to the one found for the same amplitude of the voltage disturbance at lower frequencies. In conclusion, the harmonic model ends up to be very useful when the operating frequency of the multilevel converter in the offshore substation is sufficiently higher than the output filter resonant frequency. The harmonic model seems to provide good results also for disturbances at frequencies sufficiently below the resonant frequency, at least for clusters of few turbines. Finally, the harmonic model developed in this project could be used to perform an harmonic susceptibility study of the DC power collection grid in an early stage of the network project. In a later stage is recommended to consider the switching model of the converters and the approximate frequency dependent model by curve fitting described in chapter 4 for the cables.

6.3 Future Work

Results of this project leave space to great margin of improvement both in the control design of the SRC # converter and in the harmonic susceptibility study of the DC power collection grid.

First, a better controller should be implemented in order to have a better rejection of the disturbances coming from the offshore substation of the wind farm. Classical control techniques are not likely to be applied for this converter with good results. The consecutive passages from discrete time to continuous time domain and viceversa lead to cumulative errors that turn out to be relevant. Thus, it is recommended to build a controller directly in the discrete time domain, using robust control techniques, like predictive control, in order to design a controller whose response is at least as fast as the SRC#. Only afterwards a continuous time domain model of the converter opearating in closed loop should be derived.

As further progress in the understanding of the converter, a higher power laboratory setup, than the 1 kW setup used in the project, should be set. In particular a bidirectional output voltage source is required to test the susceptibility of the converter for disturbances in the closed proximity of the resonant frequency of the output filter. This will turn out in tests of the SRC# being closer to its future implementation.

Finally, the harmonic susceptibility study of this project takes into account only the disturbances coming from the offshore wind farm substation. Other disturbances coming from different positions in the wind farm network, such as disturbances from the wind turbines, could be considered in order to have a better comprehension of the overall susceptibility to disturbances of the DC power collection grid.

Bibliography

[1] Ariola Mbistrova Andrew Ho and Giogio Corbetta. *The European offshore wind industry - key trends and statistics 2015*. 2015 edition. European Wind Energy Association, 2016.

[2] J. Beerten, S. D'Arco, and J. A. Suul. "Cable Model Order Reduction for HVDC Systems Interoperability Analysis". In: *11th IET International Conference on AC and DC Power Transmission*. Feb. 2015, pp. 1–10. DOI: 10.1049/cp.2015.0039.

[3] STUDY COMMITTEE SC C4 WG (TF) WG C4.502. *Power System Technical Performance Issues Related to the Application of Long HVAC Cables*. 2013. ISBN: 978-2-85873-251-7.

[4] Catalin Gabriel Dincan and Philip Carne Kjær. *DC-DC Converter and DC-DC conversion method, Pending Pattent Application 70059*. 2017.

[5] Robert W. Erickson and Dragan Maksimović. *Fundamentals of Power Electronics*. 2001st ed. University of Colorado Boulder, Colorado, 2001.

[6] B. Gustavsen and A. Semlyen. "Rational approximation of frequency domain responses by vector fitting". In: *IEEE Transactions on Power Delivery* 14.3 (July 1999), pp. 1052–1061. ISSN: 0885-8977. DOI: 10.1109/61.772353.

[7] Cross-Sound Cable company LLC. *Anatomy of a single-core XLPE cable, Cross-Sound Cable company*. URL: http://www.crosssoundcable.com/CableInfonew.html.

[8] Olof Martander. *DC Grid for Wind Farms*. 2002nd ed. Chalmers University of Technology, 2002.

[9] C. Meyer and R. W. De Doncker. "Design of a Three-Phase Series Resonant Converter for Offshore DC Grids". In: *2007 IEEE Industry Applications Annual Meeting*. Sept. 2007, pp. 216–223. DOI: 10.1109/07IAS.2007.40.

[10] P.Kjær, C.Bak, et al. *Power collection and distribution in medium voltage DC networks*. URL: http://www.dcc.et.aau.dk.

[11] Allen Stubberud. *Schaum's Outline of Feedback and Control Systems*. 2nd. New York, NY, USA: McGraw-Hill, Inc., 1994. ISBN: 0070170525.

[12] X. Xiang, M. M. C. Merlin, and T. C. Green. “Cost analysis and comparison of HVAC, LFAC and HVDC for offshore wind power connection”. In: *12th IET International Conference on AC and DC Power Transmission (ACDC 2016)*. May 2016, pp. 1–6. DOI: 10.1049/cp.2016.0386.

Appendix A

Derivation of the SRC # Mathematical Model

In this appendix the details of the derivation of the state space model of the SRC #, given in equations 2.12-2.18, are presented. The discrete time modeling technique is used, and a relationship between the value of state variables at the beginning of each event is found.

In the first operation sub-interval, switches T_1 and T_4 turn on. As a result, the equivalent circuit shown in the Figure 2.6a is obtained, and the following expressions are valid.

For
$t_{0(k)} \leq t \leq t_{1(k)}$ (T_1, T_4 ON)

$$v_g = L_r \frac{di_r}{dt} + v_{Cr} + v_o \tag{A.1}$$

$$i_r = C_r \frac{dv_{Cr}}{dt} \tag{A.2}$$

where:
$v_g = V_{g,0(k)}$
$v_o = V_{o,0(k)}$

By solving Equation A.1 and Equation A.2, the expressions for the voltage across the tank capacitor and the resonant current are deducted.

$$\begin{aligned} v_{Cr} =& V_{g,0(k)} - \left(V_{g,0(k)} - V_{o,0(k)} - V_{Cr,0(k)} \right) cos(\omega_r t') \\ &+ I_{r,0(k)} Z_r sin(\omega_r t') - V_{o,0(k)} \end{aligned} \tag{A.3}$$

$$i_r = \frac{1}{Z_r}\left(V_{g,0(k)} - V_{o,0(k)} - V_{Cr,0(k)}\right) sin(\omega_r t') + I_{r,0(k)} cos(\omega_r t') \tag{A.4}$$

where

$Z_r = \sqrt{\frac{L_r}{C_r}}$

$\omega_r = \frac{1}{\sqrt{L_r C_r}}$

$t' = t - t_{0(k)}$

The current starts to oscillate at the resonant frequency until it reaches zero, causing the natural turn off of the IGBTs. This time instant is point out as $t_{1(k)}$. The relationship between the state variables at the beginning and at the end of $(T_1, T_4)ON$ subinterval is therefore:

when $t = t_{1(k)} \Rightarrow t' = t_{1(k)} - t_{0(k)}$, $v_{Cr}(t_{1(k)}) = V_{Cr,1(k)}$, and $i_r(t_{1(k)}) = 0$

$$\begin{aligned} V_{Cr,1(k)} =& V_{g,0(k)} - \left(V_{g,0(k)} - V_{o,0(k)} - V_{Cr,0(k)}\right) cos(\omega_{rs}\beta_k) \\ &+ I_{r,0(k)} Z_r sin(\omega_{rs}\beta_k) - V_{o,0(k)} \end{aligned} \tag{A.5}$$

$$0 = \frac{1}{Z_r}\left(V_{g,0(k)} - V_{o,0(k)} - V_{Cr,0(k)}\right) sin(\omega_r t_{1(k)}) + I_{r,0(k)} cos(\omega_r t_{1(k)})$$

$$tan(\omega_{rs}\beta_k) = -\frac{Z_r I_{r,0}}{V_{g,0(k)} - V_{o,0(k)} - V_{Cr,0(k)}} \tag{A.6}$$

where

$\omega_s(t_{1(k)} - t_{0(k)}) = \beta_k$

$\omega_r(t_{1(k)} - t_{0(k)}) = \frac{\omega_r}{\omega_s}\beta_k = \omega_{rs}\beta_k$

Next, the diode bridge is reverse biased until the switch T_3 turns on, at the time instant $t_{2(k)}$. No current will flow through the tank, and so the voltage across the capacitor keeps the same value, until this time instant. According to the pulse removal control technique:

$$\omega_s \cdot (t_{2(k)} - t_{1(k)}) = \omega_s \cdot (\frac{T_r}{2} - \beta_k) = \frac{\pi - \beta}{\omega_{rs}} \tag{A.7}$$

when $t = t_{2(k)} \quad \Rightarrow \quad v_{Cr}(t_{2(k)}) = V_{Cr,2(k)} = V_{Cr,1(k)} \quad , \quad i_r(t_{3(k)}) = I_{r,3(k)} = I_{r,2(k)} = 0$

At the time instant $t_{2(k)}$, IGBT T_3 is pulsed and starts to conduct. As a result, zero voltage is applied to the turbine side of the converter and a negative current starts to increase. The equivalent circuit of Figure 2.6b is valid, thus Equation A.1 is still valid, while by Kirchoff's voltage law:

For $t_{2(k)} \leq t \leq t_{3(k)}$ (D_1, T_3 ON)

$$0 = L_r \frac{di_r}{dt} + v_{Cr} - v_o \tag{A.8}$$

By the solution of these equations:

$$v_{Cr}(t') = \left(V_{o,1(k)} + V_{Cr,1(k)}\right) cos(\omega_r t') - V_{o,1(k)} \tag{A.9}$$

$$i_r(t') = -\frac{1}{Z_r}\left(V_{o,1(k)} + V_{Cr,1(k)}\right) sin(\omega_r t') \tag{A.10}$$

$t' = t - t_{2(k)}$

Therefore, at the time instants $t_{3(k)}$:

when $t = t_{3(k)} \quad \Rightarrow \quad t' = t_{3(k)} - t_{2(k)} \quad , \quad v_{Cr}(t_{3(k)}) = V_{Cr,3(k)} \quad , \quad i_r(t_{3(k)}) = I_{r,3(k)}$

also,

$\omega_s(t_{3(k)} - t_{2(k)}) = \alpha_k$

$\omega_r(t_{3(k)} - t_{2(k)}) = \frac{\omega_r}{\omega_s}\alpha_k = \omega_{rs}\alpha_k$

$$I_{r,3(k)} = -\frac{1}{Z_r}\left(V_{o,1(k)} + V_{Cr,1(k)}\right) sin(\omega_{rs}\alpha_k) \tag{A.11}$$

Replacing Equation A.5 in Equation A.11, and considering $V_{o,1(k)} = -V_{o,0(k)}$:

$$\begin{aligned} I_{r,3(k)} = \frac{1}{Z_r}(V_{o,0(k)} - V_{g,0(k)} + (V_{g,0(k)} - V_{o,0(k)} - V_{Cr,0(k)}) \cdot cos(\omega_{rs}\beta_k) \\ - I_{r,0(k)}Z_r \cdot sin(\omega_{rs}\beta_k) + V_{o,0(k)}) \cdot sin(\omega_{rs}\alpha_k) \end{aligned} \tag{A.12}$$

$$\begin{aligned} I_{r,3(k)} = &- sin(\omega_{rs}\beta_k) \cdot sin(\omega_{rs}\alpha_k) \cdot I_{r,0(k)} \\ &- \frac{1}{Z_r} cos(\omega_{rs}\beta_k) \cdot sin(\omega_{rs}\alpha_k) \cdot V_{Cr,0(k)} \\ &+ \left(\frac{2}{Z_r} sin(\omega_{rs}\alpha_k) - \frac{1}{Z_r} cos(\omega_{rs}\beta_k) \cdot sin(\omega_{rs}\alpha_k) \right) \cdot V_{o,0(k)} \\ &+ \left(-\frac{1}{Z_r} sin(\omega_{rs}\alpha_k) + \frac{1}{Z_r} cos(\omega_{rs}\beta_k) \cdot sin(\omega_{rs}\alpha_k) \right) \cdot V_{g,0(k)} \end{aligned} \tag{A.13}$$

$$\begin{aligned} V_{Cr,3(k)} = &\, Z_r \cdot sin(\omega_{rs}\beta_k) \cdot cos(\omega_{rs}\alpha) \cdot I_{r,0(k)} \\ &+ cos(\omega_{rs}\beta_k) \cdot cos(\omega_{rs}\alpha) \cdot V_{Cr,0(k)} \\ &+ (-2 \cdot cos(\omega_{rs}\alpha) + cos(\omega_{rs}\beta_k) \cdot cos(\omega_{rs}\alpha) + 1) \cdot V_{o,0(k)} \\ &+ (cos(\omega_{rs}\alpha) - cos(\omega_{rs}\beta_k) \cdot cos(\omega_{rs}\alpha)) \cdot V_{g,0(k)} \end{aligned} \tag{A.14}$$

The output current is found assuming that it is equal to its mean value during each event. A small ripple approximation is then used considering that a filter is placed on the output side of the converter.

$$\begin{aligned} i_o = \frac{1}{t_{3(k)} - t_{0(k)}} \Bigg[&\int_{t_{0(k)}}^{t_{1(k)}} \left(\frac{1}{Z_r} (V_{g,0(k)} - V_{o,0(k)} - V_{Cr,0(k)}) \cdot sin(\omega_r t) + I_{r,0(k)} \cdot cos(\omega_r t) \right) dt \\ &+ \int_{t_{2(k)}}^{t_{3(k)}} -\frac{1}{Z_r} (V_{Cr,2} - V_{o,0(k)}) \cdot sin[\omega_r (t - t_{2(k)})] dt \Bigg] \end{aligned} \tag{A.15}$$

if $\theta_s = \omega_s t \quad , \quad \gamma_k = \pi$

$$\begin{aligned} i_o = \frac{1}{\gamma_k \cdot Z_r} \Bigg[&\int_0^{\beta_k} \left((V_{g,0(k)} - V_{o,0(k)} - V_{Cr,0(k)}) \cdot sin(\omega_{rs}\theta_s) + I_{r,0(k)} \cdot cos(\omega_{rs}\theta_s) \right) d\theta_s \\ &- \int_{\frac{\pi}{\omega_{rs}}}^{\pi} (V_{Cr,1} - V_{o,0(k)}) \cdot sin[\omega_{rs}(\theta_s - \beta_k)] d\theta_s \Bigg] \end{aligned} \tag{A.16}$$

$$\begin{aligned} i_o = \frac{1}{\gamma_k \cdot \omega_{rs} \cdot Z_r} \Big\{ &Z_r \left[sin(\omega_{rs}\beta_k) + sin(\omega_{rs}\beta_k)(1 - cos(\omega_{rs}\alpha_k)) \right] \cdot I_{r,0(k)} \\ &+ [cos(\omega_{rs}\beta_k) \cdot (1 - cos(\omega_{rs}\alpha_k)) - (1 - cos(\omega_{rs}\beta_k))] \cdot V_{Cr,0(k)} \\ &+ [(cos(\omega_{rs}\beta_k) - 2) \cdot (1 - cos(\omega_{rs}\alpha_k)) - (1 - cos(\omega_{rs}\beta_k))] \cdot V_{o,0(k)} \\ &+ [(1 - cos(\omega_{rs}\beta_k)) \cdot (1 - cos(\omega_{rs}\alpha_k)) + (1 - cos(\omega_{rs}\beta_k))] \cdot V_{g,0(k)} \Big\} \end{aligned} \tag{A.17}$$

The following event $(k+1)$ is described by the same equations, but with reverse polarities, so the following choice of state variables of the state space model is advantageous:

$$x_{1(k)} = I_{r,0(k)}; \quad x_{2(k)} = V_{Cr,0(k)} \tag{A.18}$$

$$x_{1(k+1)} = -I_{r,2(k)}; \quad x_{2(k+1)} = -V_{Cr,2(k)} \tag{A.19}$$

In order to develop a continuous time model for the state variables, the time derivatives of the state variables are set equal to the incremental ratio of the discrete state variables during each event:

$$\dot{x}_i(k) = \frac{x_{i(k+1)} - x_{i(k)}}{t_{0(k+1)} - t_{0(k)}} = \frac{2}{T_s} \cdot \left(x_{i(k+1)} - x_{i(k)}\right) \tag{A.20}$$

Where T_s is the switching period.
By considering the voltage across the tank capacitor and resonant current as continuous:

$$I_{r,0(k+1)} = I_{r,3(k)}; \quad V_{Cr,0(k+1)} = V_{Cr,3(k)} \tag{A.21}$$

Substituting definitions A.18-A.19 into the expressions A.13-A.14, and by using Equation A.20, the continuous state space model of equations 2.12-2.18 is obtained. Removing the subscripts, the output equation 2.20 is obtained directly by Equation A.17.

Appendix B

Components and Equipment of the Laboratory Setup

The scaled-down system requires two voltage sources to supply the IGBT drivers and the DSP. The DC voltage source *Delta SM 300-5* supplies the front end (V_{in}) of the scaled down converter. On the turbine side (V_{out}), AC programmable source *Chroma 61511* is used for all the harmonic tests and the dynamic test in open loop. For the dynamic tests in closed loop (see Figure 5.6 (b), (c) and (d)) the DC voltage source *Keysight N8957A* is used on the output side of the converter (V_{out}) to represent the DC grid. The Table B.1 shows the rating values of the sources.

Table B.1: Required sources for the experimental work

Source	[V]	[A]	[Hz]	Model
V_{driver}	15	1	0	GW Instek GPS-4303
V_{DSP}	5	0.25	0	GW Instek GPS-4303
V_{in}	216	8	0	Delta SM 300-5
V_{out}	400	4	0	Keysight N8957A
V_{dist}	3.5	4	20 – 300	Chroma 61511

The passive elements used in the experimental work are depicted in the Table B.2. The main characteristics of the electronic devices in this scaled-down system are detailed in Table B.3. In addition, Table B.4 and Table B.5 show the used measurement equipment and the operating-point values respectively.

Table B.2: Passive elements

Component	Magnitude
C_{in}	1 mF
L_r	20 mH
C_r	1 μF
L_f	2.5 mH
C_f	1 μF
R	500 Ω
Transformer	N2/N1 = 2/1, L_m = 17 mH

Table B.3: Electronics Devices

Device	Model	Characteristics
IGBT		1200 V, 1 kA
Diode	SKKE 15/06	600V V, 14 A
Driver	2SP0320T2A0	Suitable for 1200V IGBT modules
Current Sensor	LEM LA 55-P	50 A
DSP	TMS320F28379D	200 MHz, 24 A/D, 24 PWM

Table B.4: Measurement equipment

Equipment	Model
Oscilloscope	HDO 4054
Differential voltage probe	ADP 305
Current probe	TCP0020

Table B.5: Operating point

Variable	Magnitude
P_o	547.9 W
f_{sw}	800 Hz
V_{in}	216 V
V_{out}	400 V
i_n	1.37 A